The Astrophysical Journal, 570:799–819, 2002 May 10

QUIESCENT AND FLARING STRUCTURE IN RS CANUM VENATICORUM STARS

J. Sanz-Forcada,[1] N. S. Brickhouse, and A. K. Dupree
Harvard-Smithsonian Center for Astrophysics, 60 Garden Street, Cambridge, MA 02138;
jsanz@cfa.harvard.edu, nbrickhouse@cfa.harvard.edu, adupree@cfa.harvard.edu
Received 2001 October 16; accepted 2002 January 18

ABSTRACT

Four of the most active RS CVn stars (V711 Tau, II Peg, σ Gem, and UX Ari) have been observed for a total of 3 Ms with the *Extreme Ultraviolet Explorer* satellite (*EUVE*) between 1992 and 2000 January. Flaring and quiescent states of extreme ultraviolet spectra ($\lambda\lambda$70–740) and light curves ($\lambda\lambda$75–175) have been analyzed to provide emission measure distributions (EMD) for these systems in the range log T_e(K) $\sim$ 5.6–7.4, based principally on iron lines. Flux measurements obtained with *IUE* and the *Orbiting and Retrievable Far and Extreme Ultraviolet Spectrometer* (*ORFEUS*) complete the EMD in the lower temperature range [log T_e(K) $\sim$ 4.0–5.6]. Frequent flaring activity has been found in the systems, including an increase during the rise phase by a factor of $\sim$9 in the flux of σ Gem, the largest flare enhancement observed with *EUVE*. Analyses of the *EUVE* emission in the active single star AB Dor and the low-rotation giant star β Cet are also included. The EMDs are remarkably similar among all the stars, showing a narrow enhancement or "bump" around log T_e(K) $\sim$ 6.9. These narrow bumps are apparently unrelated to rotation rate, spectral type, binarity, or evolutionary stage. Significant material is found at log T_e(K) $\gtrsim$ 7.0 for the most active stars. Modulation of the EUV flux outside of flaring occurs in four of the stars (σ Gem, V711 Tau, UX Ari, AB Dor). The electron density ranges between $N_e \sim 10^{12}$ and $\sim 10^{13}$ cm^{-3}, measured at log T_e(K) $\sim$ 7.0, and may reach higher values during flares. These densities and EMD values imply small scale sizes for emitting regions.

Subject headings: stars: coronae — stars: individual (σ Geminorum, UX Arietis, II Pegasi, V711 Tauri, AB Doradus, β Ceti) — stars: late-type — ultraviolet: stars — X-rays: stars

On-line material: color figures

1. INTRODUCTION

The arrival of the *Extreme Ultraviolet Explorer* (*EUVE*), providing access to the EUV with spectral resolution better than 0.5 Å, has made the study of individual spectral lines from coronal ions possible for a wide variety of stars different from the Sun. Atomic emission models allow construction of a continuous emission measure distribution (EMD), which reveals distributions quite different from the solar corona in active stars (Dupree et al. 1993). Following Dupree et al. (1993), Brickhouse & Dupree (1998), and Sanz-Forcada, Brickhouse, & Dupree (2001), we have applied a line-based method to calculate the EMD of several active binaries (including flaring events) and two single stars. Our models provide a comprehensive view of coronal structures in single active stars and active binaries with orbital periods of 3–20 days. The coronal models, based on strong iron lines, will also provide useful fiducial models for the analysis of spectra from *Chandra* and *XMM-Newton*.

After 8 years of *EUVE* observations, it is now possible to differentiate flaring from quiescent spectra with good statistics for some of the most active stars. Among these stars are the RS CVn systems, characterized by strong emission at UV, EUV, and X-ray wavelengths resulting from a vigorous rotationally driven magnetic dynamo (Hartmann & Noyes 1987). UX Ari, V711 Tau, σ Gem, and II Peg are among the RS CVn stars most frequently observed with *EUVE*, totaling 3 Ms of observations at the beginning of the year 2000. The four systems show photometric periods very close to their orbital periods (see Table 1), suggesting that these systems are tidally locked.

UX Ari (HD 21242) is a frequent subject of stellar activity studies, having also a long record of flare detections from radio to X-ray wavelengths. Optical spectroscopy shows a very active K0 IV star and a G5 V companion with low activity levels (Simon & Linsky 1980). Large enhancements in the intensities of lines formed in the chromosphere (by a factor of 2.5) and transition region (by a factor of 5.5) are detected during flares with respect to the quiescent levels (Simon, Linsky, & Schiffer 1980). Sixty days before the *EUVE* 1995 observations, Montes et al. (1996) observed a flare with an increase by a factor of 2.9 in the equivalent width of the broad component of the chromospheric Hα emission line.

V711 Tau (HD 22468, HR 1099) is a common target for the study of stellar coronae, with detection of flares reported by many authors. The origin of most of the activity is believed to come from a K1 IV star in a system with a G5 IV star as companion (Bopp & Fekel 1976). Enhancements in the lines detected during flares in the chromosphere (by a factor or 1.5) and transition region (by a factor of 2.3) are also believed to arise from the K1 IV star (Linsky et al. 1989). Recent studies determine the changing spot coverage of the photosphere of the K1 star, including migration of spots toward high latitudes (Donati 1999; Strassmeier & Bartus 2000), as well as variations in the photometric phase during 6 years of observations (Donati 1999).

σ Gem (HD 62044, HR 2973) contrasts with the other three RS CVn systems in the sample in that only one flare detection has been reported to date, perhaps because the

[1] Present address: Osservatorio Astronomico di Palermo G. S. Vaiana, Piazza del Parlamento 1, Palermo I-90134, Italy.

TABLE 1
STELLAR PARAMETERS

Name	HD	Spectral Type	P_{orb} (days)	P_{phot} (days)	i (deg)	N_H (cm^{-2})	d[a] (pc)	R_* ($R_\odot$)
UX Ari..........	21242	G5 V/K0 IV	6.438[b]	6.4[a]	59[c]	1.5×10^{18} [d]	50.2	1.11/5.78[c]
V711 Tau......	22468	G5 IV/K1 IV	2.838[c]	2.841[c]	33[c]	1.0×10^{18} [d]	29.0	1.3/3.9[c]
σ Gem..........	62044	K1 III + ?	19.604[e]	19.604[f]	41[e]	9.4×10^{17} [g]	37.5	9.3/?[h]
II Peg............	224085	K2 IV/M0–3 V	6.724[i]	6.718[i]	60[i]	3.0×10^{18} [d]	42.3	3.4/?[i]
AB Dor.........	36705	K1 IV	...	0.51479[j]	60:[k]	1.3×10^{18} [d]	14.9	1.0:[k]
β Cet............	4128	K0 III	...	...	60[l]	2.2×10^{18} [m]	29.4	15.1:[n]

[a] Perryman et al. 1997.
[b] Duemmler & Aarum 2001.
[c] Strassmeier et al. 1993.
[d] This work.
[e] Duemmler, Ilyin, & Tuominen 1997.
[f] Berdyugina & Tuominen 1998.;
[g] Dring et al. 1997.
[h] Nordgren et al. 1999.
[i] Berdyugina et al. 1998.
[j] Innis et al. 1988.
[k] Maggio et al. 2000.
[l] Gray 1989.
[m] Piskunov et al. 1997.
[n] Jordan & Montesinos 1991.

amount of *IUE* data available for this star is less than for the other three RS CVn systems. The spectrum of σ Gem is dominated by a primary K1 III star, with no lines observed from the companion (Strassmeier et al. 1993). Berdyugina & Tuominen (1998) found an active longitude in σ Gem and derived an activity cycle of 14.9 yr. *IUE* observations reported by Engvold et al. (1988) show rotational modulation in UV lines, but no flares were detected.

II Peg (HD 224085) is a well-known source of flares in a wide range of wavelengths, and spot coverage and activity cycles have been derived recently by Berdyugina et al. (1999) and Rodonò et al. (2000), among others. The spectra of II Peg show only a K2 IV star, and Berdyugina et al. (1998) estimated the unseen companion to be an M0–3 V star.

Two single stars, the rapidly rotating dwarf star AB Dor[2] and the evolved star β Cet, have been added to the sample in order to identify possible differences in the EMD due to binarity or age. AB Dor (HD 36705) is a frequent subject of studies in X-ray wavelengths because of its high level of activity. Moreover, Doppler imaging studies reveal complex patterns of spot activity (cf. Collier Cameron et al. 1999). Although a K1 V–IV classification is commonly adopted now, it was first classified as a pre–main-sequence star, and later revised as a zero-age main-sequence (ZAMS) star (see Maggio et al. 2000, and references therein, for a longer discussion). β Cet (HD 4128, HR 188) is a K0 III single star with an apparent low rotational velocity ($v \sin i = 4$ km s^{-1}; Fekel 1997), but with surprisingly high levels of activity in X-rays.

Although upper limits to the EMD from line-based models based on EUV spectra have been derived for V711 Tau and II Peg (Griffiths & Jordan 1998), further observations now allow determination of a better constrained EMD, and the possibility of obtaining separate spectra for flaring and quiescent stages. This allows us to determine different EMDs depending on activity levels, as was done previously for λ And (Sanz-Forcada, Brickhouse, & Dupree 2001) to document changing coronal structure. Moreover, we determine continuous EMDs in the EUV region by considering the emissivity as a function of temperature for the spectral lines (and not simply maximum values). Such full integration of the emissivity functions is necessary because the EMD of coronal structures is not smooth.

Some analysis of the light curves during flares is also presented here. EUV flare morphology generally shows a pattern consisting of a fast rise phase and slow decay that follows a power law, but sometimes this pattern does not occur. Osten & Brown (1999) analyzed the light curves of 16 RS CVn systems and sometimes found rise times comparable to or greater than the decay times. They also noted emission plateaus, or decay phases that follow a "broken power law" instead of a single power law in the RS CVn systems.

In § 2, we discuss the *EUVE* and *IUE* observations, followed by the techniques of data analysis for the light curves and spectra (§ 3.1). The six target stars are treated individually in successive sections. Comparison of our results among the stars is made in § 4, and a summary of conclusions occurs in § 5.

2. OBSERVATIONS

EUVE observations taken between 1992 October and 2000 January are used (Table 2). Some of the observations were awarded to us through the Guest Observer program, while most of them were made available through the *EUVE* Data Archive. The *EUVE* spectrographs (Bowyer & Malina 1991; Abbott et al. 1996) cover the spectral ranges 70–180, 170–370, and 300–750 Å for the short-wavelength (SW), medium-wavelength (MW), and long-wavelength (LW) spectrometers, respectively, with corresponding spectral dispersion of $\Delta\lambda \sim 0.067$, 0.135, and 0.270 Å pixel^{-1}, and an effective spectral resolution of $\lambda/\Delta\lambda \sim 200$–400. The

[2] AB Dor has a low-mass stellar companion (Guirado et al. 1997) orbiting with a period of 6.5–27.5 yr, so it is effectively a single star in its coronal characteristics.

TABLE 2
EUVE EXPOSURE TIMES (SW SPECTRUM)

Name	Start Date	Exposure Time (s)
UX Ari..........	1994 Oct 19	132071
	1995 Nov 7	381031
	1998 Aug 23	114799
V711 Tau	1992 Oct 22	62179
	1993 Sep 16	218573
	1994 Aug 24	192578
	1996 Sep 1	204964
	1998 Sep 3	153097
	1999 Sep 13	179650
σ Gem	1993 Feb 6	68183
	1998 Dec 10	205076
	1999 Dec 30	309980
II Peg	1993 Oct 1	144245
	1995 Aug 5	153221
	1998 Sep 11	122639
	1999 Oct 21	314394
AB Dor	1993 Nov 4	269830
	1994 Nov 12	142789
β Cet	1994 Sep 30	215285

Deep Survey (DS) Imager has a bandpass of 80–180 Å and is used for EUV photometry.

EUVE light curves for the targets (Figs. 1 and 2) were built from the DS image by taking a circle centered on the source and subtracting the equivalent sky background within an annulus around the center. Standard procedures were used in the IRAF package EUV version 1.9, with a time binning of 600 s. Points affected by the "dead spot" are marked as open circles in the light curves, while filled circles mark the unaffected points. The dead spot is a low-gain area of the DS detector that affects some of the observations taken in 1993 and 1994, resulting in variable levels of contamination of the signal (see Miller-Bagwell & Abbott 1995). An error bar indicating the average of the noncontaminated data is included. The variations observed in the light curves show different activity levels, including some flaring episodes. Quiescent and flaring states were identified in the light curves; vertical lines separate the different states in the light curves. Spectra binned over these selected intervals were extracted from the three spectrographs (Figs. 3–7 show the SW and MW spectra). Strong iron lines identified in the summed *EUVE* spectra of the four RS CVn systems are given in Table 3. Table 4 displays the AB Dor and β Cet fluxes.

International Ultraviolet Explorer (*IUE*) archive NEWSIPS spectra have been used to construct the EMD curve of the stars by providing lines formed at temperatures lower than those occurring in the *EUVE* spectra. Low-resolution spectra (~6 Å) covering $\lambda\lambda$1100–1950 were used for active and quiescent stages of the stars. Spectra taken during flares were frequently available. When this was not possible, spectra with the highest flux levels in the *IUE* database were selected as a "flaring sample." *IUE* line fluxes used to determine the EMD are shown in Table 5. *Orbiting Retrievable Far and Extreme Ultraviolet Spectrometers* (*ORFEUS*) data were added for UX Ari to complement the lines used in the low-temperature region of the EMD. The *ORFEUS* spectrum was taken on 1996 November 24.

3. DATA ANALYSIS

3.1. *Light Curves and Spectra*

The DS light curves of the four RS CVn stars are shown and compared with the orbital phase in Figures 1 and 2. The photometric period was used for AB Dor (Fig. 2), while no periods are available for β Cet. These will be discussed for individual stars below.

To obtain fluxes of the EUV emission lines, we first performed optimized extractions from the summed two-dimensional images by removing an averaged background evaluated on either side of the spectrum, using the software provided in IRAF and the EGODATA 1.17 reference data set. A local continuum in the spectrum itself, determined by visual inspection, was subtracted from each line where necessary. The error in the line flux is defined as $\sigma = 1/[S + B(1 + 1/n)]^{1/2}$, where S is the net signal, B is the estimated average background, and n is the oversampling ratio (i.e., the ratio of total background pixels to the number of total source spectral pixels in the image), having a value $n \sim 10$–15 in our extraction.

To correct the observed fluxes for interstellar hydrogen and helium continuum absorption, we used a ratio He I/H I = 0.09 (Kimble et al. 1993), and values for $N_{\rm H}$ calculated in different ways for each star. Frequently, the observed ratios of the Fe XVI λ335 and λ361 lines can indicate the amount of interstellar absorption, because the theoretical ratio (1.94 in photon units) is determined from fundamental atomic physics. When these line fluxes are available, they have been used to establish or corroborate hydrogen column densities to the targets. Table 1 lists the values assumed, and further discussion follows in the section for each star.

The EUV energy radiated during the three largest flares in the sample as identified by the DS observations (in UX Ari, V711 Tau, and σ Gem) has been measured by direct integration of the flux in the SW spectrum (corrected for absorption by the interstellar medium [ISM]) within the bandpass of 80–170 Å, as explained in Sanz-Forcada et al. (2001). This measured flux is corrected by the elapsed time of the flare in order to account for the time gaps present in the data stream, and then multiplied by $4\pi d^2$ (where d is the distance to the star). Finally, values in the quiescent stage were subtracted to obtain the net energy in the flare (see Table 6). This method differs from that followed by Osten & Brown (1999) as discussed by Sanz-Forcada et al. (2001).

IUE spectra show an unusually high flux level in the N V λ1240 line in some cases, relative to the fluxes of other lines formed in overlapping temperature ranges. This discrepancy is likely to arise from an overabundance of nitrogen resulting from deep mixing in the stellar convective core, as has been pointed out by Böhm-Vitense & Mena-Werth (1992) in stars with $B-V \gtrsim 0.8$, including σ Gem and β Cet. We find this abnormally high flux in UX Ari, σ Gem, AB Dor, and β Cet. Hence, this nitrogen line has not been considered for the fitting of the EMD of these stars.

The electron density in the corona of the stars at $\log T_e({\rm K}) \sim 6.9$–7.0 has been inferred from ratios of the observed fluxes (corrected for interstellar absorption) of Fe XIX λ91.02/(λ101.55 + λ109.97 + λ111.70), Fe XIX λ91.02/ (λ108.37 + λ120.00), Fe XX λ110.63/ (λ118.66 + λ121.83), Fe XXI λ102.22/λ128.73, Fe XXI λ142.16/λ102.22, and Fe XXII λ114.41/λ117.17 in the summed spectrum. Iron line emissivities were generally

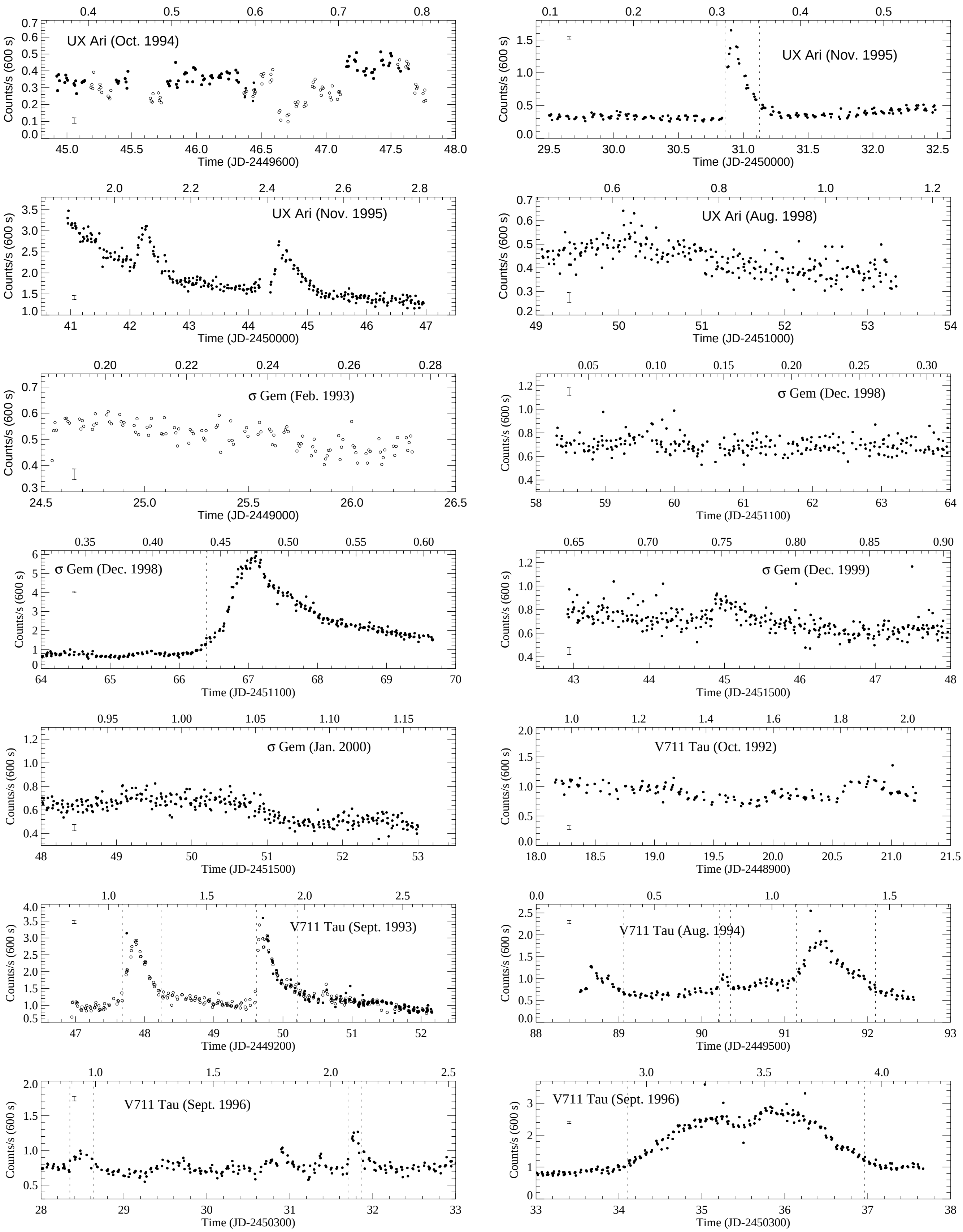

FIG. 1.—DS light curves as a function of Julian Date (*lower axis*) and orbital phase (*upper axis*). We use the convention that at orbital phase 1.0 the primary star is located behind the secondary star (see Table 1). Open circles show data affected by the dead spot, while filled circles represent unaffected data. An average error bar is shown as reference on the left side of each plot. Only points with $S/N > 5$ are plotted. Vertical lines mark the separation between quiescent and flaring stages. The bin size is 600 s.

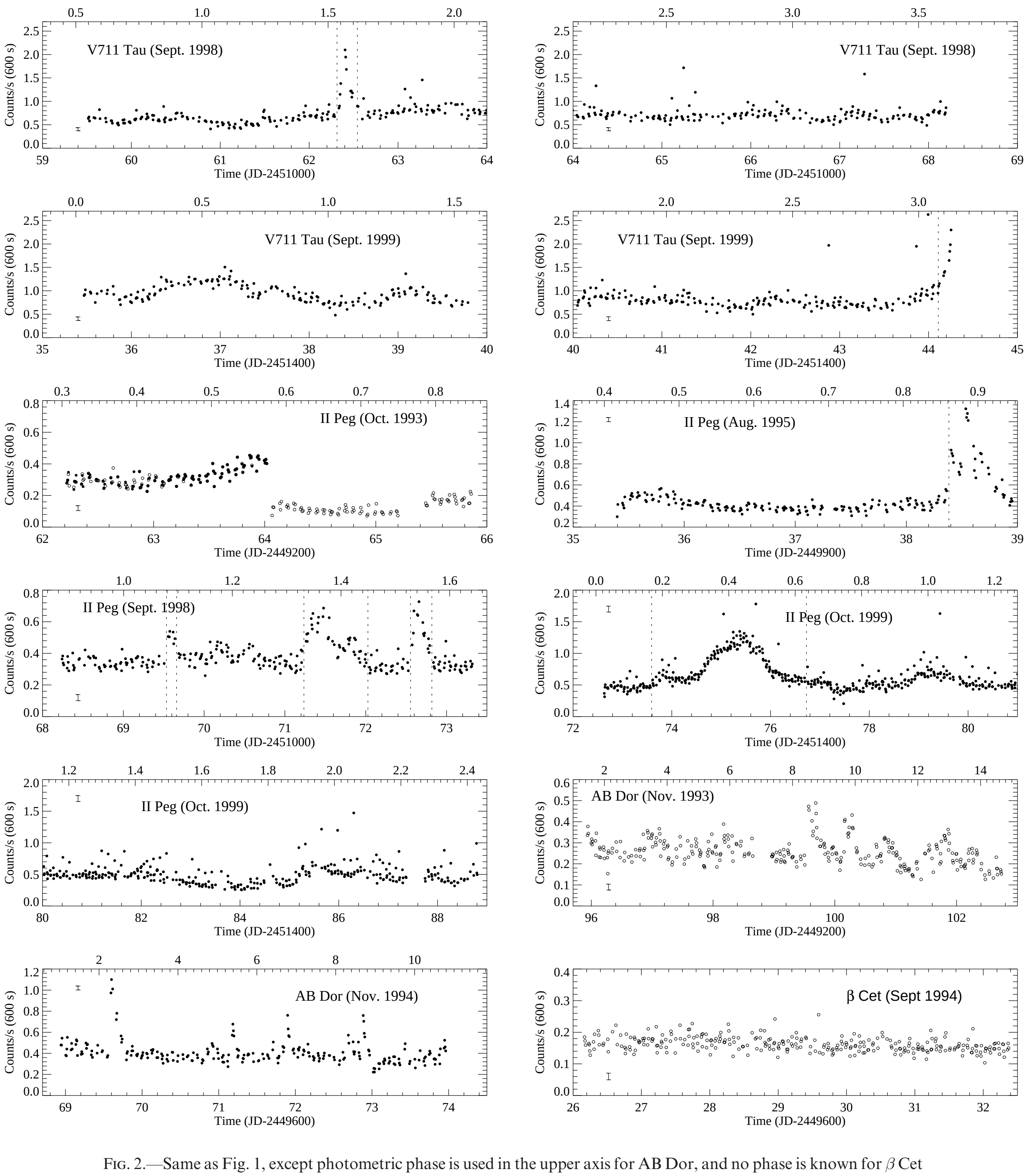

FIG. 2.—Same as Fig. 1, except photometric phase is used in the upper axis for AB Dor, and no phase is known for β Cet

computed for the densities derived in each spectrum. Atomic models for Fe XX–XXII were taken from Brickhouse, Raymond, & Smith (1995), with Fe XIX from Liedahl's HULLAC calculations (see Brickhouse & Dupree 1998).

3.2. *Emission Measure Distribution*

We performed a line-based analysis of the emission spectrum in order to calculate the EMD ($\int N_e N_{\rm H}\, dV$ cm^{-3}, where N_e and $N_{\rm H}$ are electron and hydrogen densities, in cm^{-3}) corresponding to the observed fluxes. In contrast to *ROSAT* and *ASCA* measurements, which constrain coronal models with only two or three temperatures, *EUVE* gives information on a continuous set of ionization states. In fact, all stages of iron ionization are represented from Fe IX through Fe XXIV except for Fe XVII, which has no transitions in the EUV spectral range. We used the line emissivities calculated from Brickhouse et al. (1995) for the *EUVE* iron

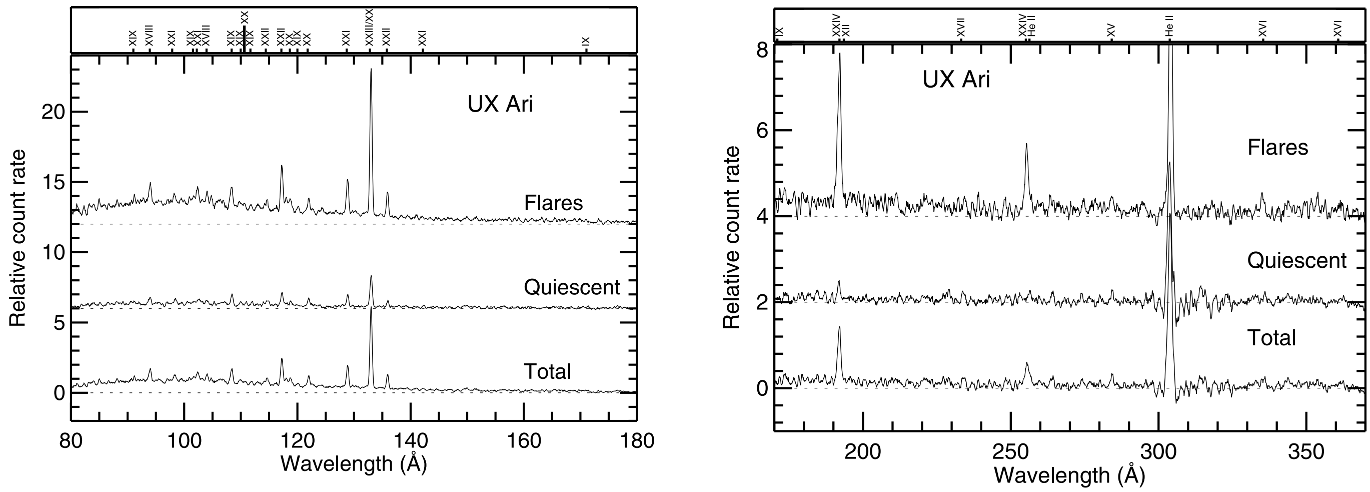

FIG. 3.—*EUVE* SW and MW spectra for UX Ari during the flare and quiescent intervals, and the summed (marked " Total ") spectra. Ion stages of iron are marked in the top panel. Spectra are smoothed by 5 pixels. Spectra for each target have been normalized to the same exposure time and then offset for display. Dotted lines indicate the zero flux level of each spectrum.

lines, based on a solar iron abundance[3] of 7.6 (Allen 1973). These emissivities have been corrected to match an iron abundance of 7.67 (Anders & Grevesse 1989). Line emissivities from Raymond (1988) are used for the (non-iron) lines formed in the UV region. Theoretical fluxes were calculated using assumed EMDs (see Dupree et al. 1993; Brickhouse & Dupree 1998, and references therein), which were then compared with the observed fluxes, in order to obtain the EMD that best fits the fluxes within a factor of 2. Iron lines severely contaminated by lines of other elements and some complex blends have been estimated by using the Astrophysical Plasma Emission Code (APEC) version 1.01 (Smith et al. 2001). These are excluded from the EMD analysis as marked in Table 3. Figures 8–10 show the EMD of summed spectra of the stars in the sample, and Figure 11 shows the comparison of summed, quiescent, and flare stages for the four RS CVn systems. The values used for the EMD are displayed in Table 7 and their quantifiable characteristics are listed in Table 8.

[3] The solar iron abundance is defined as $12 + \log(\mathrm{Fe/H})$, where Fe/H represents the ratio of iron to hydrogen by number.

3.3. *UX Ari*

3.3.1. *Light Curves*

The *EUVE* observations made of UX Ari show two interesting features: first, the presence of a giant flare in 1995 observed only in its decay phase, and originally reported by Dupree & Brickhouse (1996); and second, the slowly varying behavior of the 1998 light curve (see Fig. 1). During the 1998 observations, the light curve shows variations of $\sim$25%, with a maximum just after orbital phase 0.6. The modulation observed in the 1998 *EUVE* campaign could be due to the presence of an active region corotating with the star instead of flaring activity. Photometric and orbital periods are very close if not synchronized (see Table 1), but the

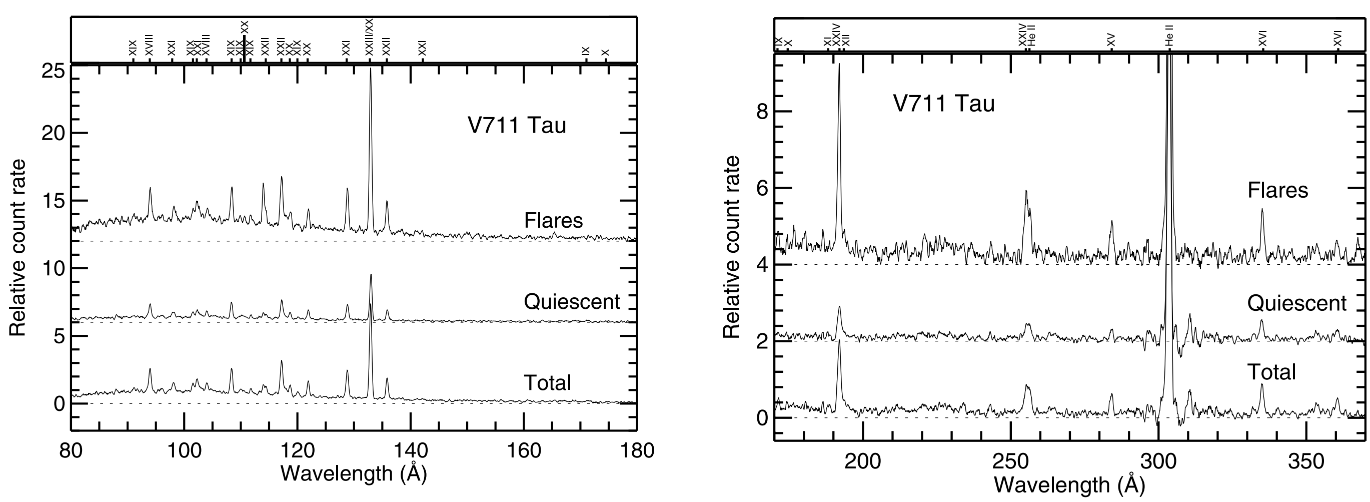

FIG. 4.—*EUVE* SW and MW spectra for V711 Tau during the flare and quiescent intervals, and the summed (marked " Total ") spectra. Ion stages of iron are marked in the top panel. Spectra are smoothed by 5 pixels. Dotted lines indicate the zero flux level of each spectrum.

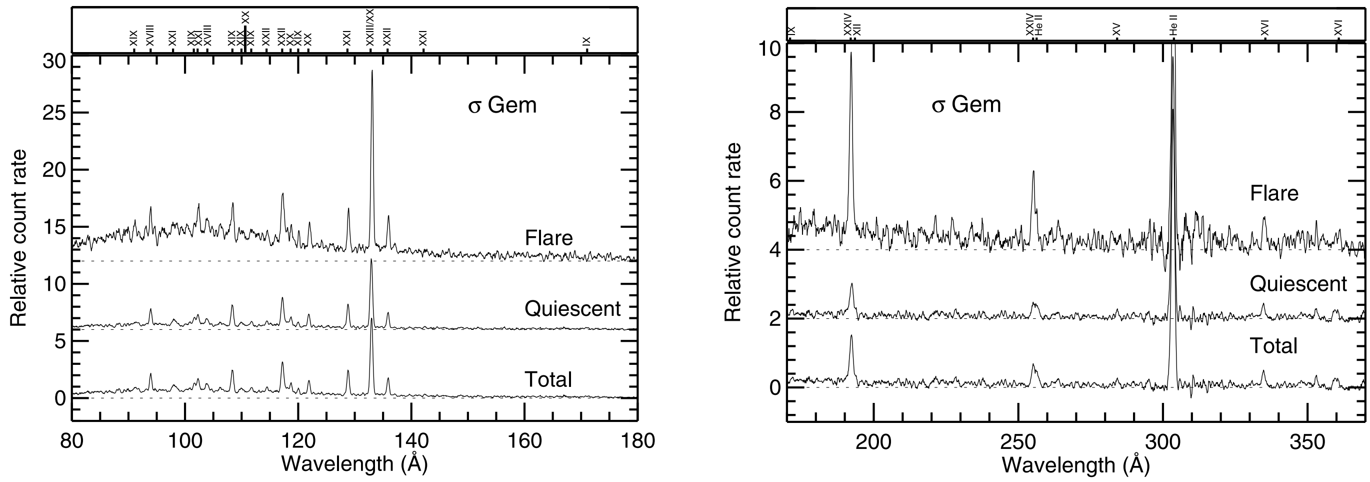

FIG. 5.—*EUVE* SW and MW spectra for σ Gem during the flare and quiescent intervals, and the summed (marked Total) spectra. Ion stages of iron are marked in the top panel. Spectra are smoothed by 5 pixels. Dotted lines indicate the zero flux level of each spectrum.

lack of data for the rest of the orbital period prevents a definitive connection between this modulation and rotational motion.

Flares occur quite frequently in UX Ari and have been recorded over a wide range of wavelengths, from radio to X-ray, including a spectroscopic Hα and He I D_3 detection 60 days before the 1995 *EUVE* flare (Montes et al. 1996), and contemporaneous optical photometric and VLBA detection reported by Henry & Hall (1997). In the portion of the 1995 giant flare observed by *EUVE*, the flux increases by a factor of 7 from the base level found in the days before the flare, and a factor of 11 above the quiescent level at the beginning of the 1995 observations. The flare decay is still on-going at the end of the observation, representing at least 144 hr (6 days) of decay. The 3 flares where rise and decay can be observed, show a typical behavior of rapid rise time (1.1 ± 0.6, 3.2 ± 1.2, and 6.2 ± 2.8 hr, respectively) and slower decay phase (9.3 ± 1.2, 9.5 ± 1.2, and 20.6 ± 1.2 hr) differing in the last two events from the values reported by Osten & Brown (1999). Our identification of the flare duration is displayed in Figure 1 and is discussed further in § 4.4.

According to the microwave data (Henry & Hall 1997), strong flare activity begins in JD 2,450,038.9583, registering multiple flare events during the rest of the observation (up to November 25, or JD 2,450,047). Their photometric data do not show such a conspicuous change, but the flare is detected at JD 2,450,039.8215, the first observation after the radio flare peak, lasting for $\sim$2 days. Assuming a simultaneous flare peak in radio and EUV, the decay time lasts at least 8 days. The net integrated energy (after removing the quiescent contribution) calculated during the large flare (including the two smaller flares during the decay) is 2.3×10^{36} ergs (total energy of 3.0×10^{36} ergs). Based on the photometric and microwave detections, this value must be a lower limit to the total *EUVE* energy produced in the flare.

3.3.2. *Spectra*

UX Ari spectra (Fig. 3) show the highest increase in the flux ratios of flaring to quiescent stages in the RS CVn sys-

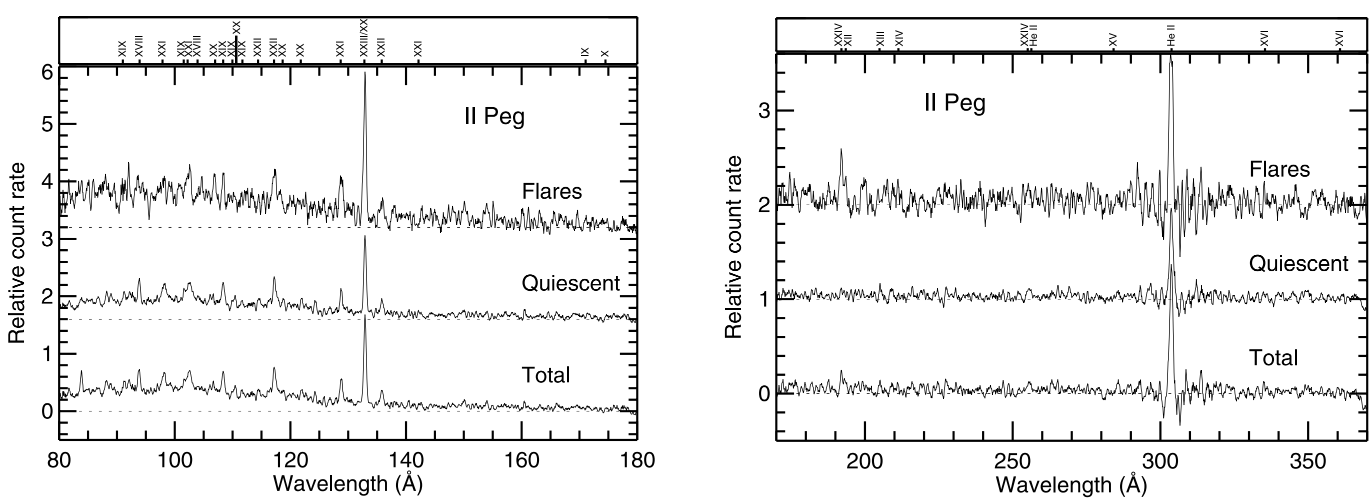

FIG. 6.—*EUVE* SW and MW spectra for II Peg during the flare and quiescent intervals, and the summed (marked " Total ") spectra. Ion stages of iron are marked in the top panel. Spectra are smoothed by 5 pixels. Dotted lines indicate the zero flux level of each spectrum.

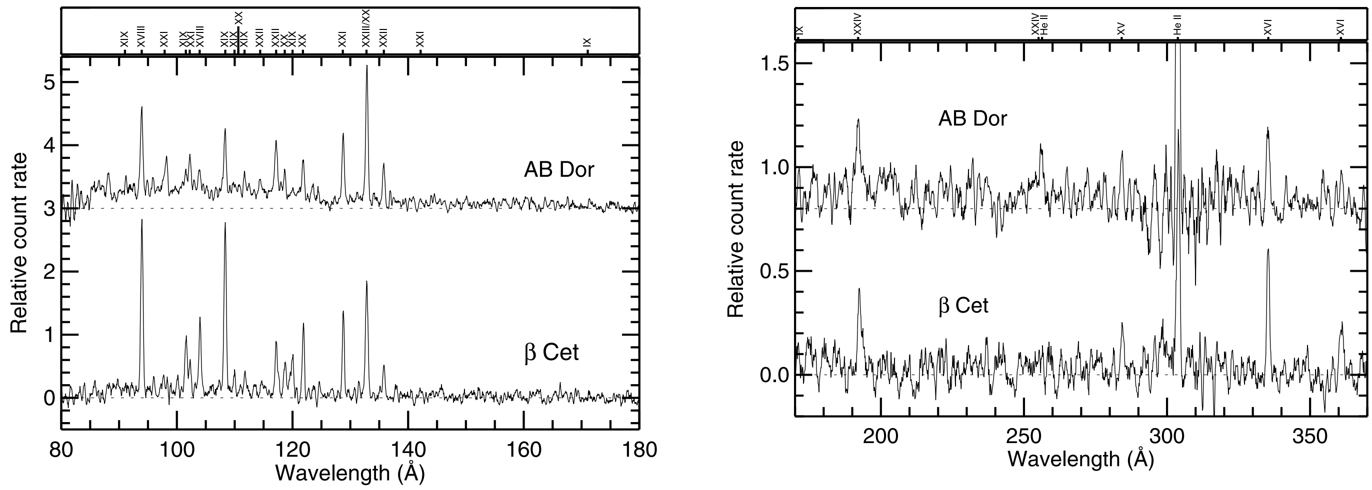

FIG. 7.—*EUVE* SW and MW spectra for AB Dor and β Cet. Ion stages of iron are marked in the top panel. Spectra are smoothed by 5 pixels. Dotted lines indicate the zero flux level of each spectrum.

tems (see Fig. 12); this increase becomes larger with increasing temperatures of line formation, reaching enhancements of factors of 4–8, the latter in Fe XXIV. This behavior is also reflected in the light curves obtained from some of the individual lines (Sanz-Forcada 2001). Enhancements by factors of 2.5 or 5.5 have been found in chromospheric and transition-region lines during a strong flare detected with *IUE* (Simon & Linsky 1980). There is an increase in the EUV continuum by a factor of 5.4 at 100 Å from quiescent to flaring spectra, similar to the enhancement found in the Fe XXIII λ132.8 and Fe XXIV λ192.0 lines.

The ratio between the fluxes of the Fe XVI λ335 and λ361 lines in the LW summed spectrum does not offer a tight bound on the hydrogen column density, namely, $\log N_{\rm H}({\rm cm}^{-2}) = 17.7^{+0.5}_{-{\rm N/A}}$. Since the estimated ratio between Fe XV and Fe XVI fits the upper limit of these values better, we have adopted a value of $\log N_{\rm H}({\rm cm}^{-2}) = 18.2$ to correct for the ISM absorption. This value is also consistent with the value of $\log N_{\rm H}({\rm cm}^{-2}) = 18.3$ estimated (Güdel et al. 1999) from *Hubble Space Telescope* (*HST*) or *EUVE* measurements of other stars close to UX Ari in direction and distance.

Electron density analysis using lines with maximum emission at $\log T_e({\rm K}) \sim 6.9$–7.0 gives values for the summed spectrum of $\log N_e({\rm cm}^{-3}) \sim 12.0$–12.9, depending on the lines ratio selected (see Fig. 13), with an average of $\log N_e({\rm cm}^{-3}) \sim 12.5 \pm 0.4$. There is no clear indication of changes in electron density during flares than for the quiescent spectrum, because the low count level for quiescent and flare spectra individually prevents an accurate determination. The values found here agree well with the estimate of $\log N_e({\rm cm}^{-3}) \sim 12.7$ reported by Güdel et al. (1999) from the Fe XXI $\lambda102.2/\lambda128.7$ flux ratio in quiescent *EUVE* spectra in 1994 and 1995.

3.3.3. *Emission Measure Distribution*

The EMD we derive from *EUVE* data (Fig. 8) shows an increasing slope over the whole temperature range covered by *EUVE*. In order to explain the high fluxes found in Fe XXIV lines, it is necessary to have an EMD with emission measure values still increasing at the end of the range at $\log T_e({\rm K}) \sim 7.4$. The EMD shows an increase between quiescent and flare stages (Fig. 11) over the whole temperature range, but these changes become more conspicuous in the region above $\log T_e({\rm K}) \sim 7.1$, where the large enhancements experienced by the Fe XXIV lines during flares have greater influence, resulting in the elevation of the EMD by 0.8 dex. Such dramatic changes consequently increase the EMD slope underlying the bump (see Table 8). Güdel et al. (1999) and Beasley & Güdel (2000) obtained three-temperature fits to the low-resolution *ASCA* spectra that also show an increase at high temperatures similar to that indicated by *EUVE*.

3.4. *V711 Tau*

3.4.1. *Light Curves*

EUVE observations of V711 Tau contain at least four strong flares, two in 1993, one in 1994 (detected also in radio wavelengths by Jones et al. 1996), and a shorter flare in 1998, as well as the beginning of a flare at the end of the 1999 campaign (reported in Ayres et al. 2001). Some smaller flarelike events are spread throughout the observations. However, in 1996 September a flux enhancement developed, reached maximum, and decayed during one orbital period, displaying an eclipse-like dip near the center of the event. The long and slow rise time as well as the behavior in the decay phase, different from the usual power law, do not resemble a typical flare. Osten & Brown (1999) suggested that the overlap of two flares might explain the light curve. But this possibility also requires unusual conditions, since the first flare has a very long rise time (~31 hr, ~40% longer than the extreme case of the large flare observed in 1998 in σ Gem), accompanied by a surprisingly low increase in flux (similar to the much shorter flares of 1993 in V711 Tau). The anomalous dip in the flare emission could result from occultation of a single (extended) flaring region on the K1 IV star for about 0.3 of an orbital period. In this case, the flaring region must be at a latitude less than 40° on the star. If the emission were optically thick, rotational modulation could also be important.

Doppler imaging reported by Strassmeier & Bartus (2000), and taken 50 days after the 1996 EUV event, shows the presence of several spots on the active star of V711 Tau.

TABLE 3

LINE FLUXES FROM THE SUMMED *EUVE* SPECTRA OF UX ARI, V711 TAU, σ GEM, AND II PEG

		UX Ari		V711 Tau		σ Gem		II Peg	
Ion	λ_{lab} (Å)	S/N	Flux at Earth (photons cm^{-2} s^{-1})	S/N[a]	Flux at Earth (photons cm^{-2} s^{-1})	S/N[a]	Flux at Earth (photons cm^{-2} s^{-1})	S/N[a]	Flux at Earth (photons cm^{-2} s^{-1})
Short-Wavelength Spectrometer									
Fe XIX[b]	91.02	6.5	1.24E−04	9.3	1.56E−04	9.2	2.08E−04	5.3	6.99E−05
Fe XVIII	93.92	13.9	3.60E−04	27.2	8.14E−04	19.6	5.56E−04	9.5	1.53E−04
Fe XXI[c]	97.88	9.3	2.04E−04	*6.0	9.13E−05	11.1	2.38E−04	9.2	1.41E−04
Fe XIX	101.55	5.4	9.09E−05	11.4	2.11E−04	12.6	2.72E−04	7.0	7.43E−05
Fe XXI[d]	102.22	11.4	2.90E−04	20.6	4.52E−04	16.6	4.38E−04	9.9	1.86E−04
Fe XVIII	103.94	8.2	1.96E−04	13.4	2.75E−04	12.9	3.36E−04	...	...
Fe XX[e]	106.98	...	...	2.9	3.93E−05	*4.1	6.23E−05	4.8	5.28E−05
Fe XIX	108.37	16.4	4.46E−04	27.9	7.17E−04	24.1	7.67E−04	10.3	1.66E−04
Fe XIX	109.97	7.8	1.66E−04	8.8	1.60E−04	8.2	1.97E−04	...	...
Fe XX	110.63	6.0	1.16E−04	3.8	5.57E−05	...	...	6.9	1.01E−04
Fe XIX	111.70	7.6	1.65E−04	8.0	1.49E−04	8.0	1.78E−04	3.3	3.38E−05
Fe XXII	114.41	11.4	2.34E−04	13.6	2.44E−04	9.7	2.21E−04	4.6	5.65E−05
Fe XXII[f]	116.28	5.0	8.79E−05	5.4	9.80E−05	...	...	4.6	4.93E−05
Fe XXII	117.17	26.9	9.74E−04	37.8	1.30E−03	33.7	1.53E−03	15.2	3.03E−04
Fe XX	118.66	12.4	2.91E−04	17.2	3.91E−04	16.2	4.32E−04	6.1	7.49E−05
Fe XIX	120.00	6.4	1.42E−04	10.1	2.25E−04	10.0	2.23E−04	...	...
Fe XX	121.83	15.1	4.59E−04	21.3	5.94E−04	19.1	6.46E−04	6.8	1.09E−04
Fe XXI	128.73	20.7	9.25E−04	33.2	1.38E−03	30.3	1.52E−03	14.4	3.33E−04
Fe XXIII[g]	132.85	47.9	3.95E−03	68.5	5.04E−03	56.5	5.48E−03	29.8	1.20E−03
Fe XXII	135.78	17.6	7.55E−04	27.3	1.14E−03	24.2	1.29E−03	11.8	2.74E−04
Fe XXI[h]	142.16	5.4	1.90E−04	7.5	2.32E−04	6.9	2.26E−04	...	...
Fe IX[i]	171.07	...	...	...	...	...	...	5.7	2.21E−04
Fe X[i]	174.53	...	...	...	...	...	...	3.3	1.25E−04
Medium-Wavelength Spectrometer									
Fe IX[i]	171.07	3.5	1.92E−04	7.3	3.78E−04	4.8	2.40E−04	...	...
Fe X[i]	174.53	...	...	5.5	2.43E−04	...	...	...	...
Fe XI	188.22	...	...	*10.6	5.90E−04	...	...	...	...
Fe XXIV[j]	192.04	22.8	3.54E−03	35.2	4.48E−03	25.9	3.33E−03	10.0	5.92E−04
Fe XII	193.51	...	...	14.1	7.30E−04	...	...	...	...
Fe XIII	204.94	...	...	...	...	...	...	*5.0	2.20E−04
Fe XIV	211.33	...	...	...	...	...	...	*3.4	1.38E−04
Fe XXIV[k]	255.10	16.1	2.72E−03	14.9	1.87E−03	17.6	2.03E−03	5.5	3.34E−04
Fe XV	284.15	8.4	7.74E−04	18.3	1.60E−03	9.6	5.58E−04	...	...
He II	303.78	39.6	1.19E−02	108.6	4.05E−02	65.9	2.05E−02	25.0	3.32E−03
Fe XVI	335.41	8.0	6.27E−04	23.4	2.03E−03	15.6	1.06E−03	4.9	1.58E−04
Fe XVI	360.80	5.7	3.45E−04	15.3	8.77E−04	11.2	5.00E−04	2.6	6.51E−05
Long-Wavelength Spectrometer									
He II	303.78	43.2	1.10E−02	103.8	3.01E−02	69.7	1.70E−02	...	...
Fe XVI	335.41	8.6	5.46E−04	25.0	2.10E−03	10.7	5.52E−04	...	...
Fe XVI	360.80	5.7	2.58E−04	22.7	1.37E−03	7.1	2.76E−04	...	...

[a] Iron lines marked with an asterisk were not used in the EMD fit. S/N columns represent the signal to noise ratio, $S/[S + B(1 + 1/n)]^{1/2}$, where S is the net signal, B is the estimated average background, and n is the oversampling ratio (i.e., the number of background pixels to the number of source pixels in the image). Here S and B are calculated for the total integrated line signal (minus continuum for SW lines) and background.

[b] Blend with Fe XXI λ91.28. Both lines are included in the measurement and modeled accordingly.

[c] Complex blend with Ne VII λ97.49, Mg VIII λ97.641, λ97.740, Mg VII λ98.031, and Ne VIII λ98.115.

[d] Blend with O VIII Hα lines between λ102.35 and λ102.51. Models indicate these lines should not contribute significantly.

[e] Blend with Ne VIII λ107.099.

[f] Potential blend with O VI λ116.349.

[g] Blend with Fe XX λ132.85. Both lines are included in measurement and modeled accordingly.

[h] Blended with Fe XXI λ142.27. Both lines are included in the measurement.

[i] These lines are near the spectrometer limits and may be difficult to measure in either SW or MW. Lack of redundant measurements indicates that the lines were weak and/or noisy.

[j] May include blend of O V ($\lambda\lambda$192.751, 192.799, 192.906), Fe XII (λ192.394), and possibly other weaker components.

[k] Nearby He II emission (λ256.317) was deblended from the Fe XXIV(λ255.10) emission.

TABLE 4

LINE FLUXES FROM THE SUMMED *EUVE* SPECTRA OF AB DOR AND β CET

Ion	λ_{lab} (Å)	AB Dor S/N[a]	AB Dor Flux at Earth (photons cm^{-2} s^{-1})	β Cet S/N[a]	β Cet Flux at Earth (photons cm^{-2} s^{-1})
Short-Wavelength Spectrometer					
Fe XIX[b]	91.02	5.3	1.06E−04	...	...
Fe XVIII	93.92	17.3	6.08E−04	17.9	1.04E−03
Fe XXI[c]	97.88	*11.0	3.02E−04	6.5	1.22E−04
Fe XIX	101.55	6.8	1.38E−04	9.9	3.67E−04
Fe XXI[d]	102.22	10.3	2.43E−04	6.5	1.95E−04
Fe XVIII	103.94	8.3	1.93E−04	11.4	4.93E−04
Fe XIX	108.37	13.8	4.15E−04	18.4	9.97E−04
Fe XIX	109.97	...	...	4.6	1.25E−04
Fe XX	110.63	4.3	8.37E−05	...	...
Fe XIX	111.70	7.1	1.58E−04	5.2	1.56E−04
Fe XXII	114.41	5.6	1.58E−04	3.7	1.04E−04
Fe XXII	117.17	14.6	5.25E−04	9.8	4.71E−04
Fe XX	118.66	7.8	2.01E−04	7.3	2.85E−04
Fe XIX	120.00	...	...	7.1	2.70E−04
Fe XX	121.83	11.1	3.45E−04	10.2	5.20E−04
Fe XXI	128.73	16.9	7.50E−04	11.3	7.19E−04
Fe XXIII[e]	132.85	24.9	1.65E−03	15.2	1.39E−03
Fe XXII	135.78	12.9	5.70E−04	6.1	3.55E−04
Fe IX[f]	171.07	4.0	2.98E−04	*1.3	1.41E−04
Medium-Wavelength Spectrometer					
Fe IX[f]	171.07	*2.8	2.66E−04	1.6	2.29E−04
Fe XXIV[g]	192.04	7.7	1.15E−03	4.6	8.63E−04
Fe XV	284.15	4.6	6.78E−04	3.1	5.99E−04
He II	303.78	16.6	6.83E−03	8.4	2.67E−03
Fe XVI	335.41	6.7	8.68E−04	6.2	1.17E−03
Fe XVI	360.80	3.3	3.05E−04	3.7	5.60E−04
Long-Wavelength Spectrometer					
He II	303.78	23.9	9.70E−03	12.4	3.93E−03
Fe XVI	335.41	7.2	9.19E−04	10.1	1.83E−03
Fe XVI	360.80	5.1	3.80E−04	6.3	8.14E−04

[a] Lines marked with an asterisk were not used in the EMD fit. S/N is the signal-to-noise ratio, described in Table 3.

[b] Blend with Fe XXI λ91.28. Both lines are included in the measurement and modeled accordingly.

[c] Complex blend with Ne VII λ97.49, Mg VIII λ97.641, λ97.740, Mg VII λ98.031, and Ne VIII λ98.115.

[d] Blend with O VIII Hα lines between λ102.35 and λ102.51. Models indicate these lines should not contribute significantly.

[e] Blend with Fe XX λ132.85. Both lines are included in measurement and modeled accordingly.

[f] These lines are near the spectrometer limits and may be difficult to measure in either SW or MW. Lack of redundant measurements indicates that the lines were weak and/or noisy.

[g] May include blend of O V ($\lambda\lambda$192.751, 192.799, 192.906), Fe XII (λ192.394), and possibly other weaker components.

These authors found a wide distribution of active regions. Thus, it is likely that active regions existed at low enough latitudes to be occulted during the 1996 September observations. Finally, the net integrated energy (subtracting the quiescent contribution) observed in this flare is 7.9×10^{35} ergs (from a total of 1.7×10^{36} ergs).

3.4.2. *Spectra*

A clear enhancement of flux in the strongest lines occurs between the quiescent and the flaring stages (see Figs. 4 and 12), with the enhancement increasing for higher iron ionization stages. The continuum is enhanced by a factor of 2.2 at 100 Å during flaring stages with respect to the quiescent spectra, similar to the changes in lines formed at high temperatures. Observations of flares in V711 Tau were recorded with *IUE* 3 days after the *EUVE* flares in 1993. Spectra in the peak of the second *IUE* flare, as well as a preflare spectrum, are used to document the changes produced in the lower temperature range [log T_e(K) $\sim$ 5.3] during the flare. Fluxes increased by up to a factor of 7.5 for the C IV 1549 line (see Table 5). Spectra from quiescent and flare stages in 1993 in the EUV observations show an increment by a fac-

TABLE 5

LINE FLUXES FROM *IUE* LOW-RESOLUTION SPECTRA

Ion	$\lambda_{feature}$[a] (Å)	S/N[a]	Flux at Earth (ergs cm^{-2} s^{-1})	S/N[b]	Flux at Earth (ergs cm^{-2} s^{-1})
UX Ari		Quiescent (SWP 56587) 1996 Jan 17, 5400 s		High Activity (SWP 42461) 1991 Sep 14, 2400 s	
O VI[c]...	1034	16.8	3.85E−13	...	...
C III....	1176	8.2	3.77E−13	6.6	5.33E−13
N V.....	1240	28.3	4.08E−13	18.9	8.00E−13
C II.....	1335	43.1	8.87E−13	26.8	1.56E−12
Si IV....	1396	28.6	2.98E−13	15.5	4.37E−13
C IV....	1549	41.1	1.15E−12	49.2	2.51E−12
V711 Tau		Quiescent (SWP 48677) 1993 Sep 18, 1770 s		Flare (SWP 48686) 1993 Sep 19, 480 s	
C III....	1176	8.9	1.06E−12	11.1	5.53E−12
N V.....	1240	15.1	4.40E−13	16.7	2.07E−12
C II.....	1335	39.7	2.62E−12	45.7	7.76E−12
Si IV....	1396	23.6	6.15E−13	40.1	4.41E−12
C IV....	1549	39.3	3.56E−12	59.0	2.69E−11
σ Gem		Quiescent (SWP 07265) 1979 Nov 29, 2400 s		High Activity (SWP 07970) 1980 Feb 17, 1800 s	
C III....	1176	17.7	1.07E−12	19.4	1.79E−12
N V.....	1240	37.0	1.17E−12	33.9	1.58E−12
C II.....	1335	49.8	1.62E−12	51.9	2.73E−12
Si IV....	1396	27.8	8.96E−13	34.6	1.08E−12
C IV....	1549	59.6	3.07E−12	51.3	4.34E−12
II Peg		Quiescent (SWP 29215) 1986 Sep 14, 10800 s		Flare (SWP 39592) 1990 Sep 6, 4500 s	
C III....	1176	7.2	1.17E−13	24.8	1.71E−12
N V.....	1240	10.2	6.19E−14	13.2	1.90E−13
C II.....	1335	21.8	2.45E−13	53.6	1.25E−12
Si IV....	1396	16.7	8.91E−14	55.3	1.16E−12
C IV....	1549	39.5	4.82E−13	63.0	5.32E−12
		AB Dor (SWP 40495) 1990 Dec 30, 5400 s		β Cet (SWP 40363) 1990 Dec 16, 2400 s	
C III....	1176	11.9	5.39E−13	6.4	4.64E−13
N V.....	1240	18.2	2.13E−13	31.5	1.18E−12
C II.....	1335	47.5	6.22E−13	33.9	7.25E−13
Si IV....	1396	26.2	2.55E−13	24.4	6.47E−13
C IV....	1549	62.8	1.33E−12	29.1	9.64E−13

[a] Includes all components of the multiplet.

[b] S/N is the signal to noise ratio, i.e., the total flux in the line (minus corresponding continuum) divided by the square root of the quadratic summation of the errors associated with each point of the line.

[c] Measurement from *ORFEUS* data includes the sum of two individual O VI lines at λ1032 and λ1037.

tor of 3.5 in the Fe XXIV λ192.04 line, and by a factor of 2.6 in the Fe XXIII λ132.85 transition. Because the *EUVE* line flux represents an average during the flare, the increase could in fact be larger, perhaps reaching an enhancement typical of the transition-region lines indicated by *IUE* measures.

The Fe XVI line ratio gives an accurate estimate of the ISM absorption, with a value of $\log N_{\rm H}({\rm cm}^{-3}) = 18.0^{+0.2}_{-0.5}$, consistent with the value reported by Murthy et al. (1987) from measurements of H Lyα. The high S/N achieved for the V711 Tau spectra allows a more accurate determination of the electron density from line ratios than for the other stars in the sample (see Fig. 13). Very good agreement exists among all diagnostics, showing a range of values of $\log N_e({\rm cm}^{-3}) \sim 12.1$–12.4 in the total spectrum, and an average value of $\log N_e({\rm cm}^{-3}) = 12.2 \pm 0.13$. Higher electron density values are suggested during flare stages [$\log N_e({\rm cm}^{-3}) = 12.4 \pm 0.4$] with respect to the quiescent spectra [$\log N_e({\rm cm}^{-3}) = 11.7 \pm 0.3$], although these values lie at the limits of the 1 σ error bars indicated by the counting statistics.

TABLE 6

ENERGIES OF LARGE FLARES

Star	Flare Start (JD)	Duration (days)	Net Energy (80–170 Å) (10^{35} ergs)
UX Ari..........	2450041.0	6.0	23.0
V711 Tau	2450334.1	2.85	7.9
σ Gem...........	2451166.4	3.3	10.2

3.4.3. *Emission Measure Distribution*

Griffiths & Jordan (1998) analyzed the EMD for V711 Tau using individual observations from the 1993 and 1994 *EUVE* campaigns, resulting in an EMD calculated with a temperature grid of $\Delta \log T_e({\rm K}) = 0.3$. They also assumed that all the line flux originated at one temperature, that of maximum emissivity. Hence, the values of the EMD obtained in this way are upper limits to the integrated EMD. In this work, all the available *EUVE* spectra for V711 Tau are collected, which improves the S/N of all the observed lines. Moreover, the whole emissivity function was evaluated for each line as described above. The general shape of the EMD is similar to the EMD estimated by Griffiths & Jordan (1998) for temperatures above $\log T_e({\rm K}) \sim 6.5$. The level of the EMD after correcting for the distance is still higher by 0.3 dex in the Griffiths & Jordan (1998) calculations. The addition of *EUVE* data allows reasonable S/N ratios to be achieved for lines formed between $\log T_e({\rm K}) \sim 5.5$ and 6.5, enabling a clear identification of a minimum in the EMD near $\log T_e({\rm K}) \sim 5.8$. The EMD for V711 Tau is the best constrained of the stars in the sample, showing remarkable agreement between calculated and observed fluxes for the majority of the lines. An estimate of the slope underlying the bump shows that it is steeper than in Griffiths & Jordan (1998). A second enhancement in the EMD $\log T_e({\rm K}) \sim 6.3$ is necessary to model the observed flux ratio of the Fe XV and Fe XVI lines. While the higher temperature enhancements are found for a range of ionization balance models (Brickhouse et al. 1995), it is not yet clear whether atomic models could account for this lower T feature. In contrast to UX Ari, the changes in the EMD due to flaring activity in V711 Tau are more modest. A slightly steeper EMD is found during the flare stages in the high-temperature range (see Table 8).

3.5. *σ Gem*

3.5.1. *Light Curves*

σ Gem shows light-curve modulation and flare events in the 1999–2000 observations and in the 1993 measurements,

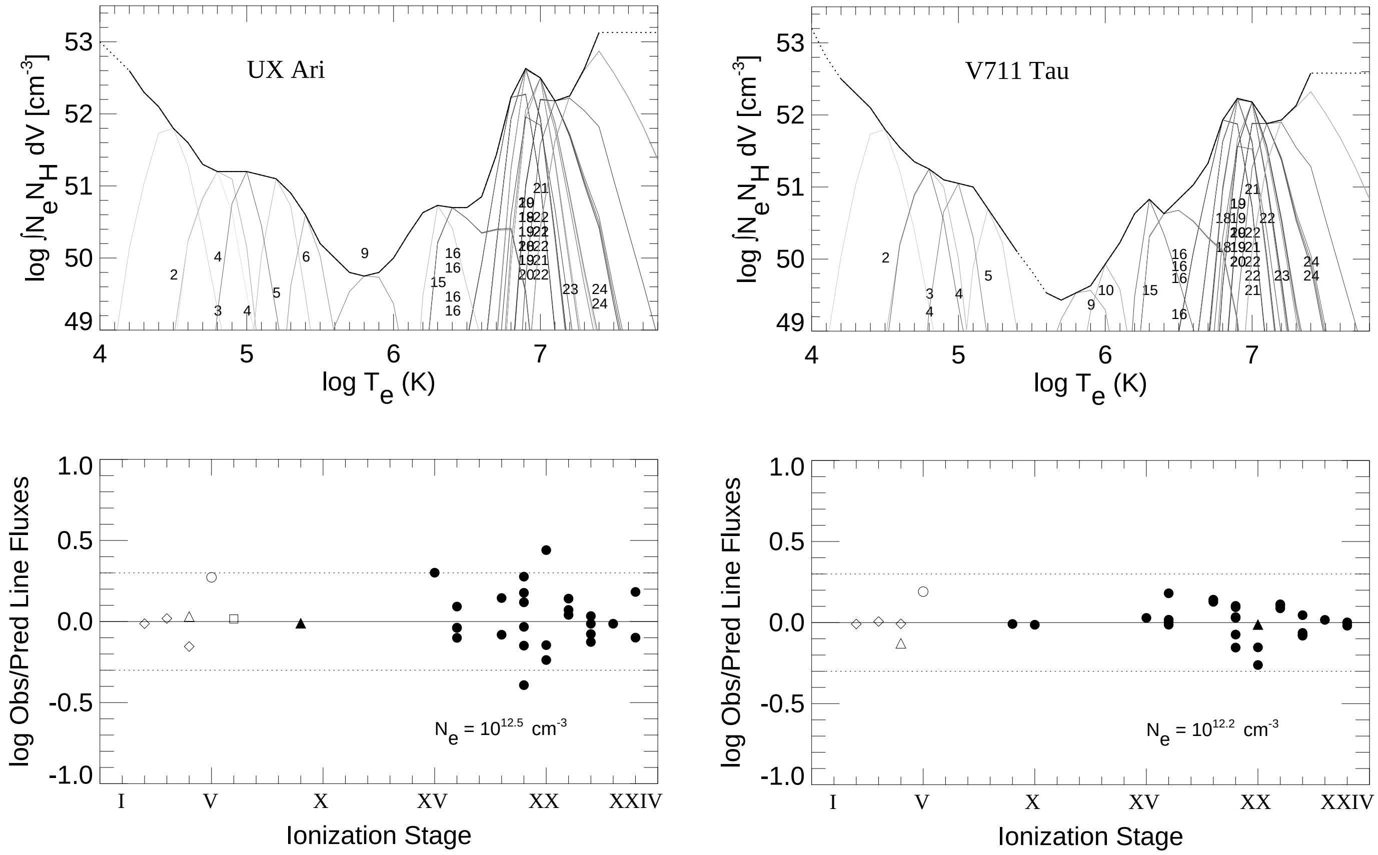

FIG. 8.—*Top*: EMD for the summed *EUVE* spectrum combined with the *IUE* quiescent spectrum for UX Ari and V711 Tau. Thin lines represent the relative contribution function for each ion (the emissivity function multiplied by the EMD at each point). *Bottom*: Observed to predicted line ratios for the ion stages in top figure with S/N > 3. The dotted lines denote a factor of 2. Filled circles represent Fe ions, open circles N, diamonds C, squares O, and open triangles Si. Filled triangles denote lines with S/N between 3 and 4. Measurements for Fe XVI are shown from the MW and LW spectra. [*See the electronic edition of the Journal for a color version of this figure.*]

although the 1993 data are severely contaminated by the dead spot. Whereas the 2000 January modulation is clear, the phase coverage is not sufficient to relate this modulation to the orbital period. This smooth decrease in the light curve (a ∼40% decrease in one day) could be produced by the rotation of an active region over the limb. In 1998 a giant flare was observed with an increase in flux by a factor of 9 with respect to pre-flare levels. This represents the largest enhancement of a flare reported in *EUVE*. This flare had a typical fast rise phase and a slow gradual decay, very similar in its characteristic decay to the 1995 UX Ari flare decay. Unlike the other three RS CVn stars in the sample, σ Gem is not known to have frequent flares, with only one flare detection reported to date, when it was observed in 1977 with *Ariel V* in X-rays (Pye & McHardy 1983). Hence, this *EUVE* flare seems to be a very atypical phenomenon because of its magnitude and duration. The net integrated energy calculated for the 1998 flare from the SW spectrum is 1.02×10^{36} ergs, while the total integrated energy is 1.40×10^{36} ergs.

3.5.2. *Spectra*

The energetic 1998 flare spectrum shows both line and continuum enhancements. The lines increase by factors of 2–4; however, the continuum levels near 100 Å increase by a factor of about 6 with respect to the quiescent spectra. The changes in the continuum are consistent with the large increase in the lines formed at high temperatures. In order to correct for the ISM absorption, we have adopted a value of $\log N_{\rm H}({\rm cm}^{-2}) = 17.9$ (Dring et al. 1997). This value is consistent with the Fe XVI λ335 and λ361 line fluxes ratio found in the summed spectrum [$\log N_{\rm H}({\rm cm}^{-2}) = 17.6^{+0.5}_{-{\rm N/A}}$].

Similar to the observations of V711 Tau, the signal achieved in the σ Gem spectra allows a good constraint for the electron density determination from the summed spectrum, with all the values within the range $\log N_e({\rm cm}^{-3}) \sim 12.2$–12.6, and an average value of $\log N_e({\rm cm}^{-3}) \sim 12.3 \pm 0.19$. Only the Fe XXII λ114.41/λ117.17 ratio fails to match the values found for the other ions. Although the line ratios are suggestive of higher densities during the flares compared with quiescence, no statistically significant difference is found.

3.5.3. *Emission Measure Distribution*

Schrijver et al. (1995) presented the first *EUVE* results for σ Gem. In our analysis of the 583 ks of data accumulated to date, the EMD is much better constrained. An enhancement is present in the EMD at $\log T({\rm K}) = 6.8$, and an increase in the slope at high temperatures occurs during the flaring stages, similar to the changes seen in UX Ari. The temperature range in which the emission measure is at its minimum [$\log T_e({\rm K}) \sim 5.5$–6.2] is poorly constrained by the low S/N of the emission lines. An increase during the flare is not well supported by the spectra.

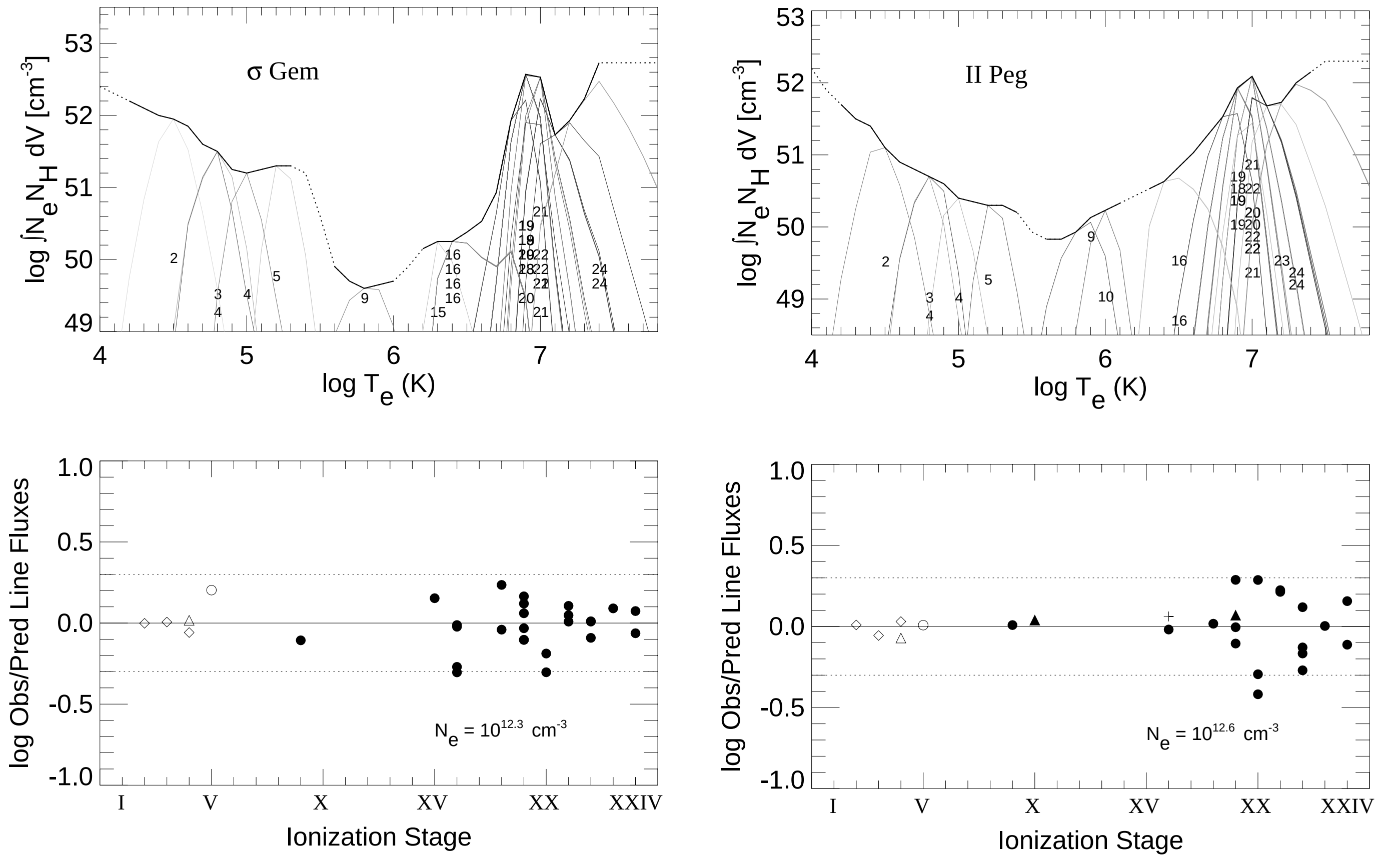

FIG. 9.—Same as in Fig. 8, but for binaries σ Gem and II Peg. In addition, the plus sign denotes a line with $S/N \leq 3$. [*See the electronic edition of the Journal for a color version of this figure*.]

3.6. *II Peg*

3.6.1. *Light Curves*

Two large flarelike events occurred in 1995 and 1999, as well as several smaller flares. While the 1995 event is a short phenomenon, showing the presence of a precursor 220 ± 30 minutes before the main peak, the 1999 flare does not exhibit a typical flare morphology. Following the 1999 big flare, some general modulation seems to be present showing an increase close to the orbital phase, $\phi_{\rm orb} \sim 1.0$ and 2.0, likely caused by the presence of a bright region lasting at least a whole orbital period. However, the flaring region ($\phi_{\rm orb} \sim 0.4$) is no longer enhanced on its second appearance. Seasonal variations were detected in the general level of flux by up to 50% in the quiescent levels. Contemporaneous photometric light curves taken during 1993, 1995, and 1998 (Rodonò et al. 2000) show a coincidence between the photometric phases when *EUVE* flares occurred in 1995 and 1998, and the minimum of the optical light curve indicating high spot coverage.

3.6.2. *Spectra*

The spectrum is dominated by iron emission and also shows very high continuum levels, even in the "quiescent" spectra. The continuum increases by a factor of ~1.6 at 100 Å during flaring episodes, similar to the enhancement of ~1.8 found in λ And (Sanz-Forcada et al. 2001). Although the spectrum of II Peg has lower S/N than the spectra for the other three RS CVn systems, the strong lines are enhanced in flares; the Fe XXIV λ192.04 line is clearly identified during flares, whereas it could not be detected in the quiescent spectra.

The determination of the ISM absorption is uncertain. We have adopted a value of $\log N_{\rm H}({\rm cm^{-2}}) = 18.5$ that is consistent with the value obtained from the ratio of the Fe XVI λ335 and λ361 lines [$\log N_{\rm H}({\rm cm^{-2}}) = 18.1^{+0.5}_{-{\rm N/A}}$], and the value derived by Huenemoerder & Baluta (1998) from *ROSAT* data [$\log N_{\rm H}({\rm cm^{-2}}) = 18.8^{+0.3}_{-0.5}$].

The electron density diagnostics from line flux ratios do not allow an accurate calculation of the values in the flaring and quiescent stages, so the summed spectrum is used. The range of values found is $\log N_e({\rm cm^{-3}}) \sim$ 12.4–13.3, with an average of 12.9 ± 0.5.

3.6.3. *Emission Measure Distribution*

Griffiths & Jordan (1998) derived an early line-based continuous EMD for this system. Their EMD was calculated in the same manner as for the case of V711 Tau, and the upper limit of the values also require a correction of 0.34 dex due to the lower distance (29 pc) adopted by these authors. We used the *Hipparcos* value of 42.3 pc.

As a consequence of the low-S/N data available for II Peg, the EMD exhibits more dispersion in the fitting than the other targets. The errors are mostly associated with the difficulties in assessing the continuum level, especially in the flare spectra. Also, uncertainties in the estimation of the ISM absorption can affect particularly the range $\log T_e({\rm K}) \sim$ 6.2–6.7. The shape of the II Peg EMD indicates a slope of 1.3, and the smallest bump enhancement of the sample [~0.5 dex at $\log T_e({\rm K}) \sim 7.0$]. In order to compare

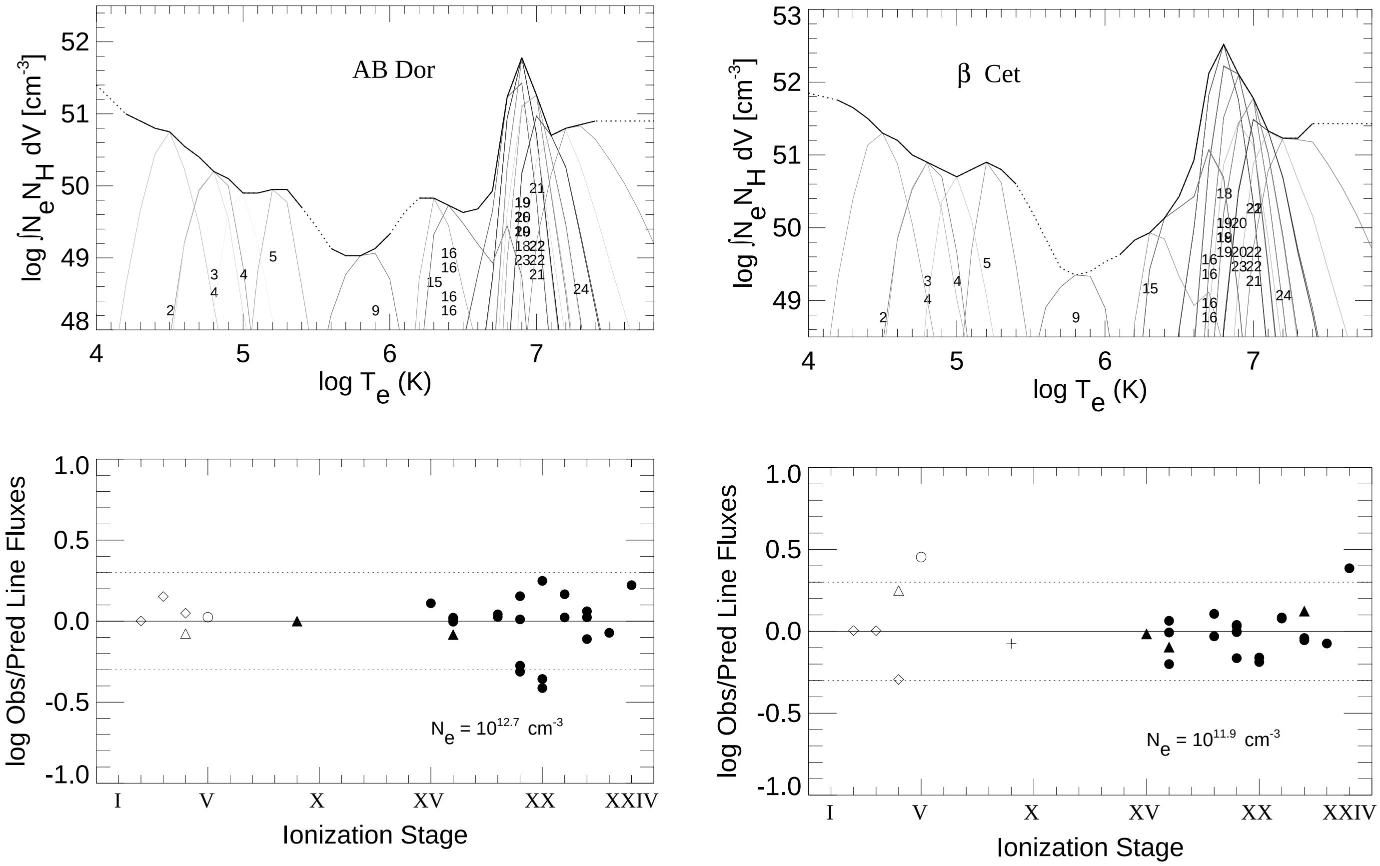

FIG. 10.—Same as Figs. 8 and 9, but for targets AB Dor and β Cet. [*See the electronic edition of the Journal for a color version of this figure.*]

the changes due to activity in the *IUE* observations, an *IUE* spectrum (Doyle et al. 1993) recorded at the peak of a flare in 1990 is used (see Table 5), which shows a conspicuous change with respect to the quiescent spectrum.

However, during the short flaring stages, the lack of enough strong lines makes the analysis of the EMD less reliable at high temperatures. The change in the *IUE* region between quiescent levels and the flare peak is outstanding,

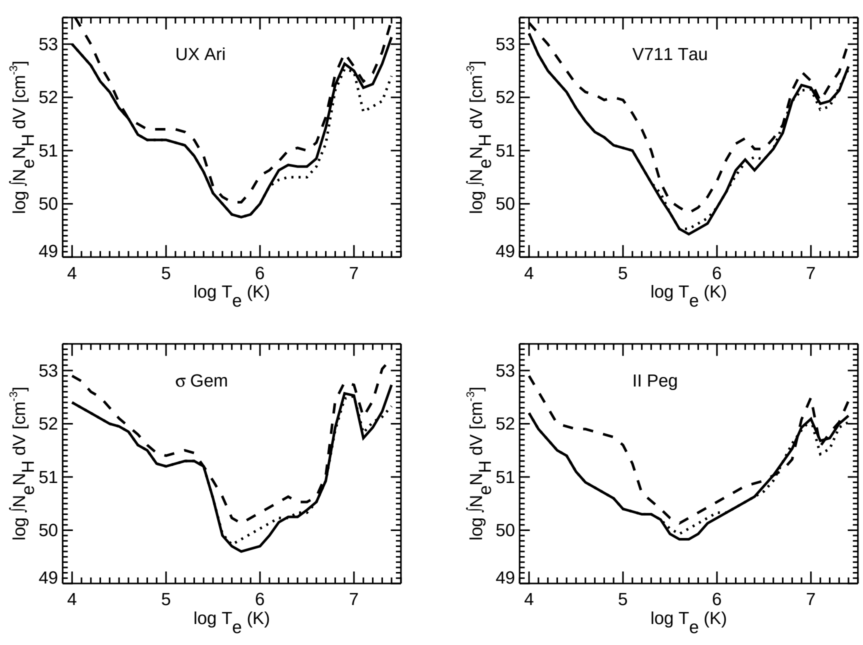

FIG. 11.—Emission measure [$\log \int N_e N_{\rm H} \, dV$ (cm^{-3})] as a function of $\log T_e$(K) for UX Ari, V711 Tau, σ Gem and II Peg during summed (*solid line*), flaring (*dashed line*), and quiescent (*dotted line*) stages. The EMD above $\log T(\mathrm{K}) = 7.4$ is uncertain (see text).

TABLE 7
EMISSION MEASURE VALUES FOR THE SUMMED (S), QUIESCENT (Q) AND FLARING (F) SPECTRA

log T (K)	$\log \int N_e N_H\, dV$ (cm^{-3})[a] UX Ari S	Q	F	V711 Tau S	Q	F	σ Gem S	Q	F	II Peg S	Q	F	AB Dor S	β Cet S
4.0......	53.00:	53.00:	53.60:	53.20:	53.20:	53.40:	52.40:	52.40:	52.90:	52.20:	52.20:	52.90:	51.40:	51.85:
4.1......	52.80:	52.80:	53.30:	52.80:	52.80:	53.20:	52.30:	52.30:	52.80:	51.90:	51.90:	52.60:	51.20:	51.80:
4.2......	52.60	52.60	53.00	52.50	52.50	53.00	52.20	52.20	52.60	51.70	51.70	52.30	51.00	51.75
4.3......	52.30	52.30	52.60	52.30	52.30	52.75	52.10	52.10	52.50	51.50	51.50	52.00	50.90	51.65
4.4......	52.10	52.10	52.30	52.10	52.10	52.50	52.00	52.00	52.30	51.40	51.40	51.95	50.80	51.50
4.5......	51.80	51.80	51.90	51.80	51.80	52.25	51.95	51.95	52.10	51.10	51.10	51.90	50.75	51.30
4.6......	51.60	51.60	51.60	51.55	51.55	52.10	51.85	51.85	51.95	50.90	50.90	51.90	50.55	51.20
4.7......	51.30	51.30	51.50	51.35	51.35	52.05	51.60	51.60	51.80	50.80	50.80	51.85	50.40	51.00
4.8......	51.20	51.20	51.40	51.25	51.25	51.95	51.50	51.50	51.60	50.70	50.70	51.80	50.20	50.90
4.9......	51.20	51.20	51.40	51.10	51.10	52.00	51.25	51.25	51.45	50.60	50.60	51.75	50.10	50.80
5.0......	51.20	51.20	51.40	51.05	51.05	51.95	51.20	51.20	51.40	50.40	50.40	51.60	49.90	50.70
5.1......	51.15	51.15	51.40	51.00	51.00	51.70	51.25	51.25	51.45	50.35	50.35	51.25	49.90	50.80
5.2......	51.10	51.10	51.35	50.70	50.70	51.40	51.30	51.30	51.50	50.30	50.30	50.70	49.95	50.90
5.3......	50.90	50.90	51.20	50.40	50.40	51.00	51.30	51.30	51.45	50.30	50.30	50.55	49.95	50.80
5.4......	50.60	50.60	50.90	50.10:	50.20:	50.40:	51.20:	51.20:	51.20:	50.20:	50.20:	50.40:	49.70:	50.60:
5.5......	50.20	50.20	50.33:	49.83:	49.83:	50.05:	50.60:	50.60:	50.93:	49.93:	50.03:	50.23:	49.43:	50.25:
5.6......	50.00	50.00:	50.13:	49.53:	49.53:	49.93:	49.90:	49.93:	50.63:	49.83:	49.93:	50.13:	49.13:	49.85:
5.7......	49.80	49.80:	50.03	49.43	49.53	49.83	49.70	49.73:	50.23:	49.83	50.03	50.23	49.03	49.45:
5.8......	49.75	49.75:	50.03	49.53	49.63	49.93	49.60	49.83:	50.13:	49.93	50.13	50.33	49.03	49.35:
5.9......	49.80	49.80:	50.23	49.63	49.73	50.13	49.65	49.93:	50.23:	50.13	50.23	50.43	49.13	49.40:
6.0......	50.00	50.00:	50.53	49.93	49.93	50.43	49.70	50.03:	50.33:	50.23	50.33	50.53	49.33	49.53:
6.1......	50.33:	50.33:	50.63:	50.23	50.23:	50.83	49.90:	50.13:	50.43:	50.33	50.33:	50.63:	49.63:	49.63:
6.2......	50.63	50.45	50.80	50.63	50.53	51.13	50.15	50.23	50.53	50.43	50.43:	50.73:	49.83	49.83
6.3......	50.73	50.50	51.00	50.83	50.78	51.23	50.25	50.23	50.63	50.53	50.53:	50.83:	49.83	49.93
6.4......	50.70	50.50	51.05	50.63	50.88	51.03	50.25	50.33	50.53	50.63	50.63:	50.88:	49.73	50.13
6.5......	50.70	50.50	51.00	50.83	50.83	51.03	50.38	50.33	50.53	50.83	50.73:	50.93:	49.63	50.43
6.6......	50.85	50.70	51.15	51.03	51.03	51.23	50.53	50.53	50.63	51.03	50.93	51.03	49.68	50.93
6.7......	51.43	51.13	51.63	51.33	51.48	51.48	50.93	50.93	51.03	51.28	51.28	51.13	49.93	52.12
6.8......	52.23	52.13	52.43	51.93	51.93	52.13	51.93	51.88	52.43	51.53	51.63	51.33	51.23	52.52
6.9......	52.63	52.53	52.83	52.23	52.13	52.48	52.57	52.47	52.78	51.93	51.88	52.08	51.78	52.11
7.0......	52.50	52.48	52.58	52.18	52.15	52.31	52.53	52.52	52.73	52.09	52.08	52.49	51.26	51.78
7.1......	52.18	51.73	52.30	51.88	51.77	51.93	51.73	51.83	52.13	51.68	51.43	51.58	50.70	51.33
7.2......	52.25	51.83	52.45	51.93	51.83	52.23	51.93	52.03	52.43	51.73	51.53	51.83	50.80	51.23
7.3......	52.63	51.93	52.85	52.13	52.18	52.48	52.23	52.13	53.03	52.00	51.93	52.03	50.85	51.23
7.4......	53.13	52.40	53.45	52.58	52.53	53.03	52.73	52.33	53.23	52.15	52.03	52.43	50.90	51.43
7.5......	53.13:	52.40:	53.45:	52.58:	52.53:	53.03:	52.73:	52.63:	53.23:	52.30:	52.43:	52.43:	50.90:	51.43:
7.6......	53.13:	52.40:	53.45:	52.58:	52.53:	53.03:	52.73:	52.63:	53.23:	52.30:	52.43:	52.43:	50.90:	51.43:
7.7......	53.13:	52.40:	53.45:	52.58:	52.53:	53.03:	52.73:	52.63:	53.23:	52.30:	52.43:	52.43:	50.90:	51.43:
7.8......	53.13:	52.40:	53.45:	52.58:	52.53:	53.03:	52.73:	52.63:	53.23:	52.30:	52.43:	52.43:	50.90:	51.43:

[a] Emission measure, where N_e and N_H are electron and hydrogen densities, in cm^{-3}. A colon indicates that the value is uncertain because few lines occur in the temperature region.

larger than the changes reported by Sarro & Byrne (2000) in II Peg and the increments noted here for V711 Tau. In addition, a slight increase of emission measure values at the hot tail of the EMD is required by the Fe XXIII and Fe XXIV emission.

A recent observation with *Chandra* (Huenemoerder, Canizares, & Schulz 2001) shows an EMD with a smoother shape at the temperatures of the bump. Although *Chandra* temperature coverage allows to achieve a more accurate calculation of the EMD at temperatures at the edge of the *EUVE* spectrometer's useful response [$\log T(\mathrm{K}) \sim 7.4$], we found that the bump reproduces the EUV and X-ray iron lines better than the EMD proposed by Huenemoerder et al. (2001). Presumably, global fitting and the inclusion of more elements and the continuum in the analysis help to smooth out the bump.

3.7. *AB Dor*

The light curves observed in the single star AB Dor (Fig. 2) do not show clear evidence of orbital modulation in the quiescent stages, but the presence of a flare in the 1993 campaign, starting at JD ∼2,449,299.7, could reveal the modulation of the flare by rotation. The presence of three peaks in consecutive orbits, separated by approximately 1.1 photometric epochs (based on photometric elements given by Innis et al. 1988), or ∼13.6 hr, could be due to a flare that rotates out of view lasting at least 34 hr. If this hypothesis is correct, this would imply a nonrigid rotation between the corona, observed in the EUV, and the photosphere. The data imply a period of 13.6 hr, ∼10% higher than the photospheric period, but consistent within statistical errors caused by the signal level and the dead-spot correction.

TABLE 8
Slope of Emission Measure at High Temperatures for Summed (S), Quiescent (Q) and Flaring (F) Intervals

Name	S	Q	F
UX Ari..........	2.31	1.78	2.18
V711 Tau	1.55	1.45	1.67
σ Gem	2.28	2.33	3.03
II Peg............	1.31	1.19	1.33
AB Dor	1.69	...	...
β Cet[a]	1.36	...	...

Note.—Slope is defined as $[d(\log\int N_e N_{\rm H}\,dV)/d(\log T)({\rm cm}^{-3}/{\rm K})]$. From emission measure values at $\log T_e({\rm K}) = \{6.5, 6.6, 6.7, 7.1, 7.2, 7.3\}$.

[a] From emission measure values at $\log T_e({\rm K}) = \{6.3, 6.4, 6.5, 7.1, 7.2, 7.3\}$.

Rotational modulation of transition region lines C III and O VI was found in 1999 observations of AB Dor (Ake et al. 2000) and would be expected in coronal emission as well.

The spectra of AB Dor (Fig. 7) are similar to the four RS CVn systems, dominated by the high-ionization iron lines with a strong continuum. The electron density derived from Fe XX, Fe XXI, and Fe XXII line ratios (Fig. 13) is very high [$\log N_e({\rm cm}^{-3}) \sim 12.3$–13.3], with an average of 12.9 ± 0.4 for $\log T_e({\rm K}) \sim 7.0$. Values of the electron density have been determined at lower temperatures, with an estimate of $\log N_e({\rm cm}^{-3}) \sim 12.3$ at $\log T_e({\rm K}) \sim 4.5$ (Brandt et al. 2001), and $\log N_e({\rm cm}^{-3}) \sim 10.4$ at $\log T_e({\rm K}) \sim 6.3$ (Güdel et al. 2001). A value of $\log N_{\rm H}({\rm cm}^{-2}) = 18.1$ is used to correct the ISM absorption; this value is obtained from the ratio between the fluxes of the Fe XVI λ335 and λ361 lines in the LW spectrum.

Mewe et al. (1996) and Rucinski et al. (1995) used global fitting techniques on *EUVE* spectra from 1993, and a preliminary line-based analysis was reported by Dupree, Brickhouse, & Hanson (1996). In our line-based continuous EMD, a bump is found similar to that derived for the other active stars, with a minimum emission measure around $\log T_e({\rm K}) \sim 5.7$, and a flatter high-temperature tail than for the four observed RS CVn systems. There are also indications of a cooler bump around $\log T_e({\rm K}) \sim 6.2$.

3.8. *β Cet*

The single star β Cet did not show any variable feature in the 1994 *EUVE* light curve (Fig. 2), and the spectra exhibit many similarities to the Capella spectra (Dupree et al. 1993; Brickhouse & Dupree 1998), because the Fe XVIII λ93.92 and Fe XIX λ108.37 lines dominate the 1994 spectrum. ISM absorption in the spectrum is corrected using a column density value of $\log N_{\rm H}({\rm cm}^{-2}) = 18.35$ (Piskunov et al. 1997). The electron density diagnostics indicate a value of $\log N_e({\rm cm}^{-3}) \sim 11.9^{+0.3}_{-0.5}$ at $\log T_e({\rm K}) \sim 7.0$ from the Fe XXI line flux ratio. Less confidence can be placed in the value of the Fe XXII line flux ratio, with larger error bars indicating $\log N_e({\rm cm}^{-3}) \sim 12.8^{+0.3}_{-0.9}$. A value of $\log N_e({\rm cm}^{-3}) \sim 11.9$ is used to evaluate the electron-density–sensitive lines for the EMD. Ayres et al. (1998) reported an EMD based on the fluxes of the EUV lines as if all the flux were emitted at the temperature of maximum emissivity, resulting in an upper limit to the EMD. We find a bump similar to that found by these authors. The distribution shows a narrow bump around $\log T_e({\rm K}) \sim 6.8$ and a flat EMD at temperatures higher than the bump according to the fit of the Fe XXIII/XX λ133 line. It must be noted that the Fe XXIV λ192.04 line in

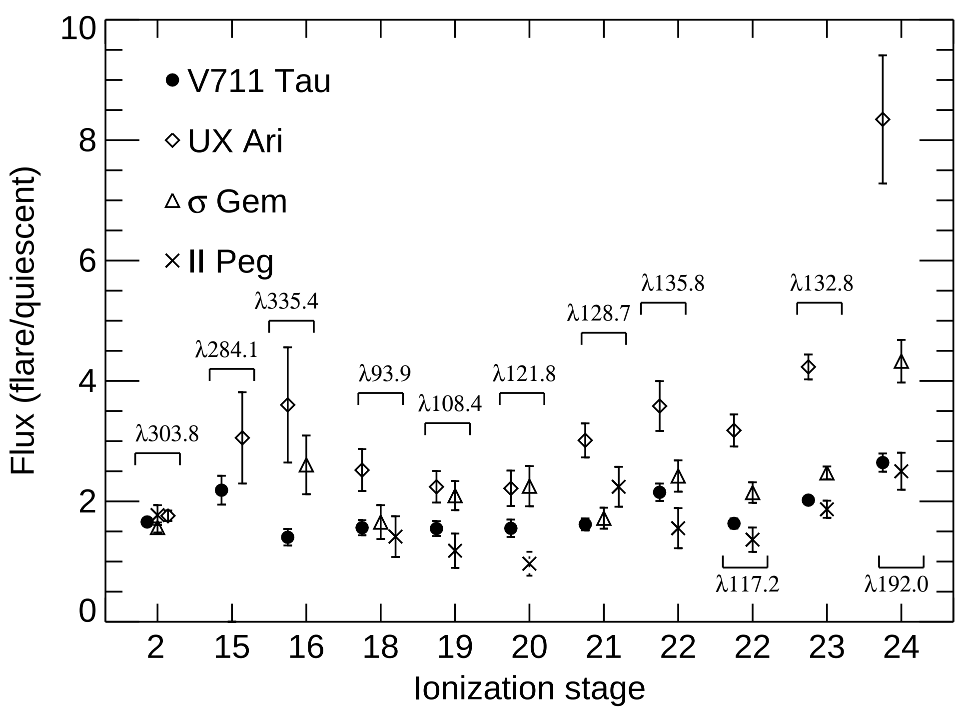

Fig. 12.—Ratio of fluxes between flaring and quiescent stages in the four RS CVn systems (except for II Peg, where the ratio for Fe XX λ122 the summed to quiescent ratio is given). Error bars are 1 σ values. Wavelengths of lines are marked (all lines are Fe lines, except He II λ303.8). The x-axis denotes the ionization stage, e.g. "15" corresponds to Fe XV. [*See the electronic edition of the Journal for a color version of this figure.*]

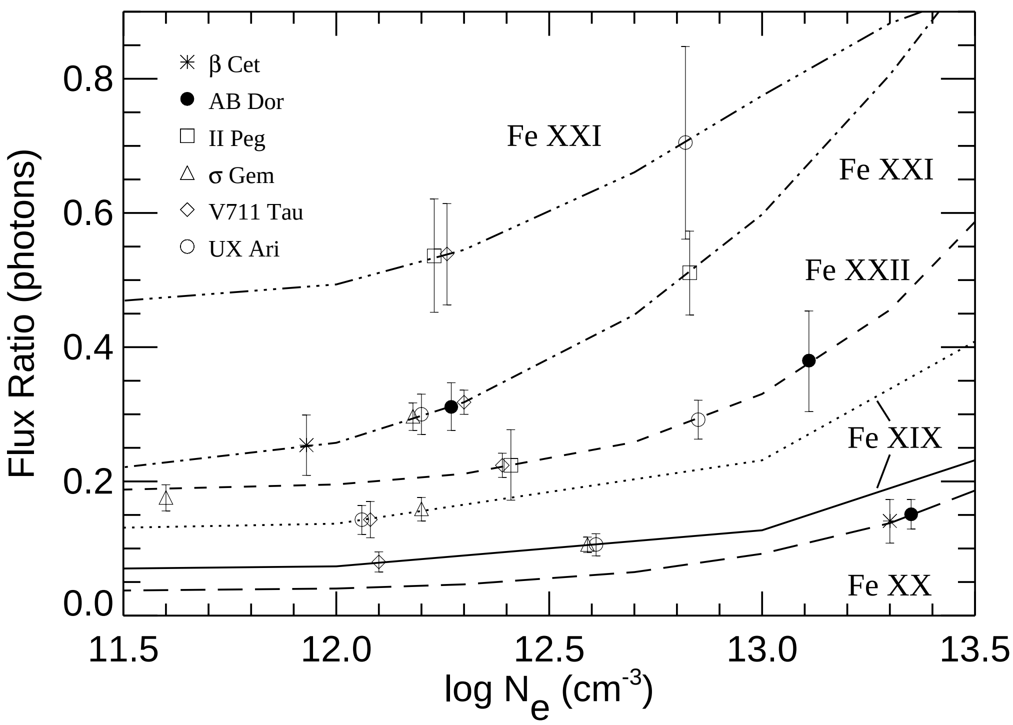

FIG. 13.—Line ratios (photons) as a function of electron density (N_e) from the summed spectra. Ratios shown (*top to bottom*) are: Fe XXI ($\lambda142.16 + \lambda142.27$)/$\lambda102.22$, Fe XXI $\lambda102.22/\lambda128.73$, Fe XXII $\lambda114.41/\lambda117.17$, Fe XIX $\lambda91.02/(\lambda101.55 + \lambda109.97 + \lambda111.70)$, Fe XIX $\lambda91.02/(\lambda108.37 + \lambda120.00)$, and Fe XX $\lambda110.63/(\lambda118.66 + \lambda121.83)$. The observed line ratios are plotted on the theoretical curves with 1 σ error bars. The flux for Fe XIX $\lambda91.02$ is obtained from the blend with Fe XXI using the Fe XXI branching ratio for $\lambda91.28$ and $\lambda102.22$. [*See the electronic edition of the Journal for a color version of this figure*.]

β Cet could be heavily contaminated by other lines, especially O V at $\sim\lambda192.8$, and so the measured flux is only an upper limit for the Fe XXIV line. Estimates of the blend caused by non-iron lines have been made using APEC version 1.01 (Smith et al. 2001) assuming solar metallicities. However, it remains puzzling that a slowly rotating evolved single giant shows such enhanced activity. It may be that the orientation is pole-on and rapid rotation is undetected.

4. DISCUSSION

4.1. *Emission Measure Distribution*

The combined spectra from *EUVE* and *IUE* allow the EMD to be defined across a wide range of temperatures, extending from the transition region to the corona. Four features are common to the EMDs of these six objects (Fig. 14): (1) the low temperature range [$\log T_e(\mathrm{K}) \lesssim 5.6$] with a decreasing slope [$d(\log \mathrm{EM})/d(\log T)(\mathrm{cm}^{-3}/\mathrm{K})$]; (2) a minimum in the range $\log T_e(\mathrm{K}) \sim 5.7$–$5.9$; (3) an increasing EMD from the minimum up to the maximum temperature observable; and (4) a narrow emission measure enhancement or "bump" around $\log T_e(\mathrm{K}) = 6.9$. These characteristics were first noted in Capella by Dupree et al. (1993).

Systematic uncertainties in the EMD may affect our interpretation of these four features. In the low-temperature region, possible abundance variations between Fe and C, O, Si, and N, in particular, can influence the determination of the EMD from *IUE* spectra and its connection to higher temperature. Furthermore, the lack of simultaneity for most of the *EUVE* and *IUE* measurements causes additional uncertainty. For V711 Tau and II Peg, measurements of this region were obtained during the peak of flares, while for UX Ari and σ Gem only fluxes at high levels of activity were calculated. At the minimum of the EMD it was not possible in all cases to observe lines formed in that temperature range with good S/N. Even in those cases where there are observable lines, this minimum is not very well constrained. The increasing EMD from minimum to maximum shows a steep slope in all cases, as shown in Table 8. The table includes

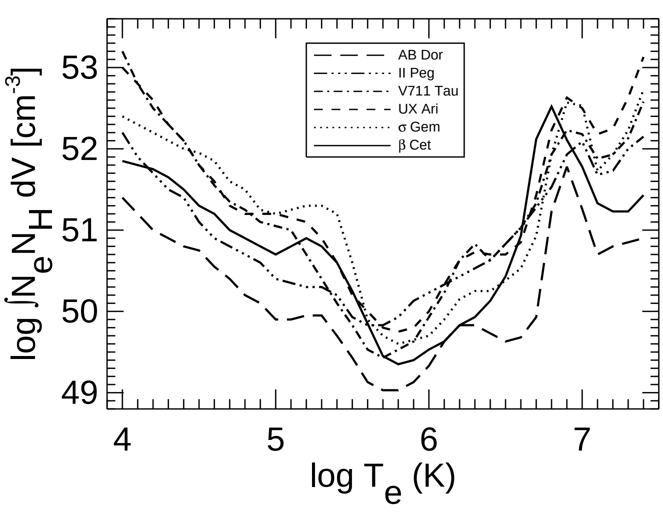

FIG. 14.—Comparison of the EMD for the summed spectra for all the stars in this sample. [*See the electronic edition of the Journal for a color version of this figure*.]

quiescent and flaring stages for the four RS CVn system and shows that the slope appears to becomes steeper during the flaring stages. The difficulty of measuring Fe XV and Fe XVI lines during quiescence makes this conclusion somewhat tentative. In addition, the uncertainties associated with the determination of the hydrogen column density can influence the comparison of slopes among these stars. This slope is sensitive to the line flux for Fe XV and Fe XVI ions, which are subject to the largest correction for the ISM. V711 Tau has the best-constrained value.

In order to test the consistency of the bump observed at $\log T_e(\mathrm{K}) \sim 6.9$ with the observational uncertainties, we have randomly varied the observed fluxes by $\pm 1\ \sigma$ in the V711 Tau summed spectra, for all lines of Fe XV–XXIV. Then we made a new fit for 10 new sets of data changed in this form. The family of new EMD curves shows a spread of $\sim$0.3 dex at $\log T_e(\mathrm{K}) \sim 6.6$ and $\log T_e(\mathrm{K}) \sim 7.3$, and $\sim$0.2 dex at $\log T_e(\mathrm{K}) \sim 6.9$. The spread in EMD values appears to be inversely proportional to the number of spectral lines in a given temperature interval. However, the bump remains a feature of the EMD in all simulations.

The EMD's of these stars show in all six cases the remarkable presence of a persistent bump around $\log T_e(\mathrm{K}) \sim 6.9$. The bump temperature remains stable independent of activity levels. The presence of this bump is also independent of binarity or rotational period. β Cet is a single star and AB Dor has a noninteracting companion. The bump, well documented in rapidly rotating stars, persists even for low apparent rotation rates, such as β Cet. A second bump might be present around $\log T_e(\mathrm{K}) \sim 6.2$ in some of the stars in the sample, reminiscent of the solar corona. However, this second peak is less well determined because of the paucity of lines. Recently, Reale, Peres, & Orlando (2001) estimated the EMD of the Sun observed as a star, using observations from *Yohkoh*. The estimated EMD shows a peak around $\log T_e(\mathrm{K}) \sim 6.1$, but flaring events create an additional bump near $\log T_e(\mathrm{K}) \sim 7.0$. Although transient and relatively small, this bump is reminiscent of those found in the stars in our sample. The presence of this bump in the EMD of the flaring Sun (Peres et al. 2000; Reale et al. 2001) points to the possibility that many solar-like flares are responsible for EMD bumps in active stars.

Some changes are found in the four RS CVn systems in the emission measure values due to activity levels, showing not only an increase in the EMD during flares over the whole temperature range, but also a tendency toward a steeper slope at high temperatures. In σ Gem and UX Ari, where the flaring spectra are dominated by one giant flare, the hot "tail" of the EMD [$\log T_e(\mathrm{K}) \gtrsim 7.0$] registers the largest increase. The EMD is very well constrained for temperatures between $\log T_e(\mathrm{K}) \sim 6.5$ and 7.0, and the hot EMD tail is needed to reproduce the fluxes of the Fe XXIII and Fe XXIV lines. While the *EUVE* spectra do not constrain the detailed shape of the EMD tail (X-ray spectra, in particular Fe XXV and possibly Fe XXVI lines, would be needed), it is present in all four RS CVn systems discussed here, as well as in σ^2 CrB and VY Ari (Sanz-Forcada, Brickhouse, & Dupree 2002, in preparation). The changes observed in the EMD during the flares affect the whole EMD by raising the amount of material at all temperatures, including the bump. This suggests that the bump is a structure intrinsic to the active corona, whether it is quiescent or flaring. Solar-like flares are not easily detected because of the low time resolution resulting from binning *EUVE* DS counts in order to obtain sufficient statistics to identify a flaring event. Changes during flares in the lower temperature range covered by *EUVE* [$\log T_e(\mathrm{K}) \lesssim 6.3$] are more uncertain, and more lines with good statistics are needed to better define the EMD curve.

The overall coronal structure presented by these stars and those included in Sanz-Forcada et al. (2002, in preparation) suggests contributions from at least two kinds of structures (presumably magnetic loops) that are more stable than others. Quiet stars like the Sun are dominated by solar-like loops, with temperatures peaking at $\log T_e(\mathrm{K}) \sim 6.3$ and lower densities [$\log N_e(\mathrm{cm}^{-3}) \sim 9$–10.5], which are well approximated by magnetic loop structures. In contrast, more active stars, such as AB Dor and V711 Tau, have a distinctly different dominant structure, with temperatures near $\log T_e(\mathrm{K}) \sim 6.9$ and much higher densities [$\log N_e(\mathrm{cm}^{-3}) \gtrsim 12$]. Heating by microflare events also produces a bump in the solar EMD at high temperatures (Klimchuk & Cargill 2001), but the densities modeled to date are far less than observed. The structure of a magnetic loop that might generate a bump in the EMD such as those found near $\log T_e(\mathrm{K}) \sim 6.9$ seems not to be a static loop with the "classic" fixed cross section. Other features need to be introduced, such as expanding cross sections (Schrijver, Lemen, & Mewe 1989; Griffiths & Jordan 1998) or mass flows along loops (Hussain et al. 2001), but these models also fail to produce the high electron densities observed, as well as the height of the bump. Flaring events could solve the mystery of the high electron densities found at $\log T_e(\mathrm{K}) \sim 7.0$ in these stars. However, the EMD bump (found near the same temperatures as the high-density measurements) is ubiquitous and apparently stable in a wide variety of stars. Moreover, the quiescent density is normally quite high, but is documented in several objects to increase further during large flaring events.

4.2. *Electron Density*

High electron densities are prevalent in these coronae, with values ranging from $\log N_e(\mathrm{cm}^{-3}) = 12$ to 13.5 at $\log T_e(\mathrm{K}) \sim 7.0$. Both single stars (AB Dor and β Ceti) and binary systems show similar high densities. Magnetic fields up to 1000 G are required to balance the electron pressures to maintain such densities in a corona. Densities of $\log N_e(\mathrm{cm}^{-3}) \gtrsim 12$ are also found at the peak of some flares in the Sun (Phillips et al. 1996). In the systems with better S/N, V711 Tau and σ Gem, an increase in the electron density during flaring stages can be identified as compared to quiescent stages (Table 9 and Sanz-Forcada 2001), similar to λ And (Sanz-Forcada et al. 2001). Emitting volumes responsible for the increases seen in the EMD during flaring stages show values similar to those found in λ And, with 2.1–4.2×10^{26} cm^3 assuming $\log N_e = 13$ (Table 9). This scenario is consistent with an increased amount of material concentrated in small volumes during flaring stages. The emitting volumes are higher for the giant flares. High densities are observed for systems with different spectral type and luminosity class, suggesting that dense magnetic structures represent a fundamental characteristic of stellar coronae. In combination with values of the EMD, the scale of the emitting material at $\log T(\mathrm{K}) = 6.8$–7.0 can be estimated. In all cases (see Table 9), the values are substantially less than a stellar radius. But it must be considered that the relationship between scale size and filling factor cannot be

TABLE 9

EMITTING VOLUMES IN THE BUMP AND INCREASE IN VOLUME DURING FLARES

	QUIESCENT				FLARES				FLARE−QUIESCENT
STAR	log EMD[a] (cm^{-3})	log N_e (cm^{-3})	V (cm^{-3})	$V^{1/3}$ (R_*)	log EMD[a] (cm^{-3})	log N_e (cm^{-3})	V (cm^{-3})	$V^{1/3}$ (R_*)	ΔV[b] (cm^{-3})
UX Ari..........	52.38	12.7	1.2×10^{27}	0.003[c]	52.61	12.6	3.2×10^{27}	0.004[c]	4.2×10^{26}
V711 Tau	52.07	11.7	5.8×10^{28}	0.014[c]	52.31	12.4	4.0×10^{27}	0.006[c]	2.1×10^{26}
σ Gem	52.29	12.2	9.7×10^{27}	0.003	52.65	12.7	2.2×10^{27}	0.002	3.8×10^{26}
II Peg.............	51.86	13.0	9.1×10^{25}	0.002	51.97	12.6	7.4×10^{26}	0.004	2.4×10^{26}
AB Dor.........	51.42	12.9	5.2×10^{25}	0.005	...	...	...	...	...
β Cet	52.25	12.4	3.5×10^{27}	0.0014	...	...	...	...	...

[a] Average of log $\int N_e N_{\rm H}\, dV$ at log T(K) = 6.8–7.0. Values at log T(K) = 6.7–6.9 are used for β Cet.

[b] Increase in volume produced in the bump [log T(K) = 6.9 in UX Ari, V711 Tau, and σ Gem; log T(K) = 7.0 in II Peg] during flares, calculated assuming log N_e (cm^{-3}).

[c] Volume attributed to the active K0 IV star in UX Ari and to the K1 IV star in V711 Tau.

determined without knowing the geometry of the emitting structures.

4.3. *Light Curves*

Flares identified in the DS data show the general pattern of short rise time and long power-law decay for longer period systems; however, short-period ($P_{\rm orb} \lesssim 3$ days) systems exhibit some unusual effects for long-lasting flares ($\gtrsim 0.5 P_{\rm orb}$). The overall behavior is consistent with the Osten & Brown (1999) data set, although the longest rise times found by these authors are not consistent with our findings.

The rise times for the sample of Osten & Brown (1999) range from 1.0 to 58.2 hr. By examining light curves for a range of time bins, we find that instead of requiring the longer rise times found by Osten & Brown (1999) ($\gtrsim 16$ hr), the rise phase is not always unambiguously determined. Some events show separate precursors, or the possibility of rotational modulation during the flare rise. There are additional ambiguities depending on the definition of the flare onset time or the preflare quiescent level. Furthermore, the measurement of the rise time is complicated by gaps in the data due to the satellite orbit.

For example, we (Sanz-Forcada et al. 2001) do not corroborate the longest rise time found by Osten & Brown (1999) (in λ And on 1993 August 3 with a reported 58 hr rise time), given our criterion that a statistically meaningful flux enhancement must occur as the signature of flare onset. We find that the 1997 September 11 flare of AR Psc (Sanz-Forcada 2001), as well as the 1996 September 7 flare on V711 Tau discussed in § 3.4.1, present similar difficulties in isolating a single flare and measuring a rise time. We find rise times of ~6 and ~5 hr, respectively, for the flares in UX Ari on 1995 November 22 (see Fig. 1), and in λ And on 1997 August 7, in contrast to their reported rise times of 15.5 and 15.9 hr. Short precursor events prior to the main peak of the flares appear to occur in II Peg, UX Ari, and V711 Tau. Other flares, such as the one detected in σ Gem in 1998, do not show a precursor. The possible relationship between the observed precursor events and the impulsive phase identified in some EUV solar flares is discussed in Sanz-Forcada et al. (2001).

Furthermore, not all flare decay times can be unambiguously determined. Osten & Brown (1999) find eight flares that are better fitted with two decay phases, but three of them do not show two clear decays (Sanz-Forcada et al. 2001; Sanz-Forcada 2001), and the remaining five originate in systems with period less than 3 days (and thus subject to possible rotational modulation). As discussed previously, a flare near its peak in V711 Tau appears to be eclipsed.

As with flares, the quiescent light curve may be affected by rotation, eclipse, small-scale flaring, and the appearance and disappearance of active regions, such that the locations of emitting regions and their extensions above the disk are difficult to infer. Brickhouse & Dupree (1998) have shown evidence for rotational modulation of an active region on the primary star of the contact binary 44ι Boo, further supported by phase-dependent Doppler shifts of X-ray lines with *Chandra* (Brickhouse, Dupree, & Young 2001). Effects of rotational modulation of X-ray and EUV light have been noted in several stars during eclipses, as in AR Lac, CF Tuc, or Algol (Ottmann & Schmitt 1994; Christian et al. 1996; Siarkowski et al. 1996; Schmitt 1998; Schmitt & Favata 1999); but evidence of rotational modulation not necessarily related to eclipses has also been reported in AB Dor, V711 Tau, AR Lac, EK Dra, and DH Leo (Ake et al. 2000; Kürster et al. 1997; Drake et al. 1994; Ottmann & Schmitt 1994; Güdel et al. 1995; Stern & Drake 1996). We find marginal evidence of rotation of active regions as identified by the light modulation in II Peg, UX Ari, σ Gem, and AB Dor.

Finally, V711 Tau exhibits a short-term variability on the order of 10–12 hr. Similar variations are found in a light curve reported by Pallavicini (2001) taken with *BeppoSAX* in 1998, partly simultaneous with the *EUVE* observations.

4.4. *Spectral Changes During Flares*

Spectra of the four RS CVn systems are similar, showing the presence of strong lines of Fe XVI and Fe XVIII–XXIV. Lower ionization stages of iron, Fe IX to Fe XV, are also detected in most cases. Figure 12 shows a ratio of flare to quiescent values of selected line fluxes for the four RS CVn systems. The EUV fluxes are averaged over the flaring events, and not simply taken at the peaks of the flares. Note that the Fe XXIV 192 Å line is barely detectable in UX Ari and not detectable at all in II Peg during the quiescent stages, but becoming very strong for the flare spectra (see Figs. 3 and 6).

The analysis of the spectra reveals conspicuous differences between the flare and quiescent stages. Flux enhancements during flares are largest for the highest ionization states. A substantial increase in the general continuum level is found during flares in all four systems. The observed continuum changes are comparable to the increases found in the fluxes of lines formed at the highest temperatures (Fe XXIII λ132.8 and Fe XXIV λ192.0). As discussed in Sanz-Forcada et al. (2001a), such an increase in the continuum would be caused mainly by bremsstrahlung from plasma at $\log T_e(\mathrm{K}) \gtrsim 6.7$.

The spectra show features similar to other RS CVn stars with high levels of activity, such as λ And (Sanz-Forcada et al. 2001). In contrast to the λ And spectra, the UX Ari, V711 Tau, and σ Gem spectra contain relatively higher continuum levels and larger line enhancements in some lines during the flaring stages. The observed enhancements in all the strong Fe lines during flares are consistent with the increase in the amount of hot material, producing larger EMD by at least a factor of 1.5–2.

The two giant flares observed in UX Ari and σ Gem show even larger increases in the EMD at the highest temperatures [$\log T(\mathrm{K}) \gtrsim 7.2$]. Only for the case of V711 Tau can we compare the increases in UV and EUV line fluxes, for which an *IUE* flare is coincident with *EUVE* flare. While the EUV line fluxes increase by a factor of roughly 2, some UV line fluxes show significantly larger increases, with C IV increasing by more than a factor of 7.

The energies that we measure (Table 6) in the region of 80–170 Å are only a small fraction ($\leq$20%) of the total thermal X-ray flux from 1 to 200 Å, as shown by modeling the flare EMD with APEC (Smith et al. 2001). Thus, the giant flares observed here could be an order of magnitude larger in radiative energy—and clearly substantially larger than solar flares, which are believed to range from 10^{29} to 10^{32} ergs in X-radiation (Moore et al. 1980).

5. CONCLUSIONS

1. Emission measure distributions (EMDs) derived for RS CVn stars (V711 Tau, II Peg, σ Gem, and UX Ari) and two single stars (AB Dor and β Cet) are remarkably similar, showing the presence of a local enhancement of the EMD over a restricted temperature range (the "bump") near $\log T_e(\mathrm{K}) \sim 6.8$–7.0. This enhancement remains constant in temperature regardless of the activity level. Coronal structure, as indicated by the EMD, thus appears independent of binarity, orbital or rotational period, and gravity within the parameters of our target stars.

2. Fe XIX–XXII line flux ratios, formed at $\log T_e(\mathrm{K}) \sim 7$ and measured in the total spectra, indicate high electron densities [$\log N_e(\mathrm{cm}^{-3}) \gtrsim 12$]. In conjunction with the EMD values, the scale sizes implied by these densities are substantially less than a stellar radius.

3. Flaring events isolated spectroscopically for the first time cause a general increase in the EMD of a factor of ~2, with highest temperatures [$\log T_e(\mathrm{K}) \sim 7.4$] increasing by as much as an order of magnitude. Increased electron density by a factor of 5 during flares may occur in V711 Tau. The possible "occultation" of a flare in V711 Tau suggests that the originating region lies at a latitude less than 40° on the active K1 IV star.

This research is supported in part by NASA grants NAG5-7224, NAG5-11093, and NAG5-3550, and CXC contract NAS8-39073 to the Smithsonian Astrophysical Observatory. J. S. F. is grateful for support in part by the Predoctoral Program of the Smithsonian Astrophysical Observatory, and the Real Colegio Complutense at Harvard University. This research has made use of the SIMBAD database, operated at CDS, Strasbourg, France, and of data obtained through the High Energy Astrophysics Science Archive Research Center On-line Service, provided by the NASA/Goddard Space Flight Center. This research has also made use of NASA's Astrophysics Data System Abstract Service.

REFERENCES

Abbott, M. J., Boyd, W. T., Jelinsky, P., Christian, C., Miller-Bagwell, A., Lampton, M., Malina, R. F., & Vallerga, J. V. 1996, ApJS, 107, 451
Ake, T. B., Dupree, A. K., Young, P. R., Linsky, J. L., Malina, R. F., Griffiths, N. W., Siegmund, O. H. W., & Woodgate, B. E. 2000, ApJ, 538, L87
Allen, C. W. 1973, Astrophysical Quantities (3rd ed.; London: Athlone Press)
Anders, E., & Grevesse, N. 1989, Geochim. Cosmochim. Acta, 53, 197
Ayres, T. R., Brown, A., Osten, R. A., Huenemoerder, D. P., Drake, J. J., Brickhouse, N. S., & Linsky, J. L. 2001, ApJ, 549, 554
Ayres, T. R., Simon, T., Stern, R. A., Drake, S. A., Wood, B. E., & Brown, A. 1998, ApJ, 496, 428
Beasley, A. J., & Güdel, M. 2000, ApJ, 529, 961
Berdyugina, S. V., Berdyugin, A. V., Ilyin, I., & Tuominen, I. 1999, A&A, 350, 626
Berdyugina, S. V., Jankov, S., Ilyin, I., Tuominen, I., & Fekel, F. C. 1998, A&A, 334, 863
Berdyugina, S. V., & Tuominen, I. 1998, A&A, 336, L25
Böhm-Vitense, E., & Mena-Werth, J. 1992, ApJ, 390, 253
Bopp, B. W., & Fekel, F. C. 1976, AJ, 81, 771
Bowyer, S., & Malina, R. F. 1991, in Extreme Ultraviolet Astronomy, Proc. First Berkeley Colloq. on Extreme Ultraviolet Astronomy, ed. R. F. Malina & S. Bowyer (New York: Pergamon), 397
Brandt, J. C., et al. 2001, AJ, 121, 2173
Brickhouse, N. S., & Dupree, A. K. 1998, ApJ, 502, 918
Brickhouse, N. S., Dupree, A. K., & Young, P. R. 2001, ApJ, 562, 75
Brickhouse, N. S., Raymond, J. C., & Smith, B. W. 1995, ApJS, 97, 551
Christian, D. J., Drake, J. J., Patterer, R. J., Vedder, P. W., & Bowyer, S. 1996, AJ, 112, 751
Collier Cameron, A., et al. 1999, MNRAS, 308, 493
Donati, J. 1999, MNRAS, 302, 457
Doyle, J. G., Mathioudakis, M., Murphy, H. M., Avgoloupis, S., Mavridis, L. N., & Seiradakis, J. H. 1993, A&A, 278, 499
Drake, J. J., Brown, A., Patterer, R. J., Vedder, P. W., Bowyer, S., & Guinan, E. F. 1994, ApJ, 421, L43
Dring, A. R., Linsky, J., Murthy, J., Henry, R. C., Moos, W., Vidal-Madjar, A., Audouze, J., & Landsman, W. 1997, ApJ, 488, 760
Duemmler, R., & Aarum, V. 2001, in ASP Conf. Ser. 223, Cool Stars, Stellar Systems, and the Sun, ed. R. J. García López, R. Rebolo, & M. R. Zapatero Osorio (San Francisco: ASP), CD 1397
Duemmler, R., Ilyin, I. V., & Tuominen, I. 1997, A&AS, 123, 209
Dupree, A. K., & Brickhouse, N. S. 1996, BAAS, 188, 7103
Dupree, A. K., Brickhouse, N. S., Doschek, G. A., Green, J. C., & Raymond, J. C. 1993, ApJ, 418, L41
Dupree, A. K., Brickhouse, N. S., & Hanson, G. J. 1996, in Proc. IAU Colloq. 152, Astrophysics in the Extreme Ultraviolet, ed. S. Bowyer & R. F. Malina (Dordrecht: Kluwer), 141
Engvold, O., et al. 1988, A&A, 192, 234
Fekel, F. C. 1997, PASP, 109, 514
Gray, D. F. 1989, PASP, 101, 1126
Griffiths, N. W., & Jordan, C. 1998, ApJ, 497, 883
Güdel, M., Linsky, J. L., Brown, A., & Nagase, F. 1999, ApJ, 511, 405
Güdel, M., Schmitt, J. H. M. M., Benz, A. O., & Elias, N. M. 1995, A&A, 301, 201
Güdel, M., et al. 2001, A&A, 365, L336
Guirado, J. C., et al. 1997, ApJ, 490, 835
Hartmann, L. W., & Noyes, R. W. 1987, ARA&A, 25, 271
Henry, G. W., & Hall, D. S. 1997, Inf. Bull. Variable Stars, 4512, 1
Huenemoerder, D. P., & Baluta, C. 1998, in ASP Conf. Ser. 154, Cool Stars, Stellar Systems, and the Sun, ed. R. A. Donahue & J. A. Bookbinder (San Francisco: ASP), 1070
Huenemoerder, D. P., Canizares, C. R., & Schulz, N. S. 2001, ApJ, 559, 1135

Hussain, G. A. J., van Ballegooijen, A. A., Jardine, M., & Collier Cameron, A. 2001, in Stellar Coronae in the *Chandra* and *XMM-Newton* Era, ed. J. Drake & F. Favata (Noordwijk: ASP), in press
Innis, J. L., Thompson, K., Coates, D. W., & Evans, T. L. 1988, MNRAS, 235, 1411
Jones, K. L., Brown, A., Stewart, R. T., & Slee, O. B. 1996, MNRAS, 283, 1331
Jordan, C., & Montesinos, B. 1991, MNRAS, 252, 21P
Kimble, R. A., Davidsen, A. F., Long, K. S., & Feldman, P. D. 1993, ApJ, 408, L41
Klimchuk, J. A., & Cargill, P. J. 2001, ApJ, 553, 440
Kürster, M., Schmitt, J. H. M. M., Cutispoto, G., & Dennerl, K. 1997, A&A, 320, 831
Linsky, J. L., Neff, J. E., Brown, A., Gross, B. D., Simon, T., Andrews, A. D., Rodono, M., & Feldman, P. A. 1989, A&A, 211, 173
Maggio, A., Pallavicini, R., Reale, F., & Tagliaferri, G. 2000, A&A, 356, 627
Mewe, R., Kaastra, J. S., White, S. M., & Pallavicini, R. 1996, A&A, 315, 170
Miller-Bagwell, A., & Abbott, M. 1995, *EUVE* Guest Observer Data Products Guide
Montes, D., Sanz-Forcada, J., Fernandez-Figueroa, M. J., & Lorente, R. 1996, A&A, 310, L29
Moore, R., et al. 1980, in Solar Flares, ed. P. Sturrock (Boulder: Colorado Assoc. Univ. Press), 341
Murthy, J., Henry, R. C., Moos, H. W., Landsman, W. B., Linsky, J. L., Vidal-Madjar, A., & Gry, C. 1987, ApJ, 315, 675
Nordgren, T. E., et al. 1999, AJ, 118, 3032
Osten, R. A., & Brown, A. 1999, ApJ, 515, 746
Ottmann, R., & Schmitt, J. H. M. M. 1994, A&A, 283, 871
Pallavicini, R. 2001, in ASP Conf. Ser. 223, Cool Stars, Stellar Systems, and the Sun, ed. R. J. García López, R. Rebolo, & M. R. Zapatero Osorio (San Francisco: ASP), 377
Peres, G., Orlando, S., Reale, F., Rosner, R., & Hudson, H. 2000, ApJ, 528, 537
Perryman, M. A. C., et al. 1997, A&A, 323, L49
Phillips, K. J. H., Bhatia, A. K., Mason, H. E., & Zarro, D. M. 1996, ApJ, 466, 549
Piskunov, N., Wood, B. E., Linsky, J. L., Dempsey, R. C., & Ayres, T. R. 1997, ApJ, 474, 315
Pye, J. P., & McHardy, I. M. 1983, MNRAS, 205, 875
Raymond, J. C. 1988, in Hot Thin Plasmas in Astrophysics, ed. R. Pallavicini (NATO ASI Ser. C, 249; Dordrecht: Kluwer), 3
Reale, F., Peres, G., & Orlando, S. 2001, ApJ, 557, 906
Rodonò, M., Messina, S., Lanza, A. F., Cutispoto, G., & Teriaca, L. 2000, A&A, 358, 624
Rucinski, S. M., Mewe, R., Kaastra, J. S., Vilhu, O., & White, S. M. 1995, ApJ, 449, 900
Sanz-Forcada, J. 2001, Ph.D. thesis, Univ. Complutense (Madrid)
Sanz-Forcada, J., Brickhouse, N. S., & Dupree, A. K. 2001, ApJ, 574, 1079
Sarro, L. M., & Byrne, P. B. 2000, A&A, 355, 227
Schmitt, J. H. M. M. 1998, in ASP Conf. Ser. 154, Cool Stars, Stellar Systems, and the Sun, ed. R. A. Donahue & J. A. Bookbinder (San Francisco: ASP), 463
Schmitt, J. H. M. M., & Favata, F. 1999, Nature, 401, 44
Schrijver, C. J., Lemen, J. R., & Mewe, R. 1989, ApJ, 341, 484
Schrijver, C. J., Mewe, R., van den Oord, G. H. J., & Kaastra, J. S. 1995, A&A, 302, 438
Siarkowski, M., Pres, P., Drake, S. A., White, N. E., & Singh, K. P. 1996, ApJ, 473, 470
Simon, T., & Linsky, J. L. 1980, ApJ, 241, 759
Simon, T., Linsky, J. L., & Schiffer, F. H. 1980, ApJ, 239, 911
Smith, R. K., Brickhouse, N. S., Liedahl, D. A., & Raymond, J. C. 2001, ApJ, 556, 91
Stern, R. A., & Drake, J. J. 1996, in Proc. IAU Colloq. 152, Astrophysics in the Extreme Ultraviolet, ed. S. Bowyer & R. F. Malina (Dordrecht: Kluwer), 135
Strassmeier, K. G., & Bartus, J. 2000, A&A, 354, 537
Strassmeier, K. G., Hall, D. S., Fekel, F. C., & Scheck, M. 1993, A&AS, 100, 173